



# 1 Importance of ice elasticity in simulating tide-induced grounding 2 line variations along prograde bed slopes

3 Natalya Maslennikova<sup>1</sup>, Pietro Milillo<sup>1,2</sup>, Kalyana Nakshatrala<sup>1</sup>, Roberto Ballarini<sup>1</sup>, Aaron Stubblefield<sup>3</sup>, Luigi Dini<sup>4</sup>

4 <sup>1</sup>Department of Civil & Environmental Engineering, University of Houston, TX, USA

5 <sup>2</sup>German Aerospace Center (DLR), Microwaves and Radar Institute, Munich, Germany

6 <sup>3</sup>Thayer School of Engineering, Dartmouth College, Hanover, NH, USA

7 <sup>4</sup>Italian Space Agency (ASI), Matera, Italy

8 *Correspondence to:* Natalya Maslennikova (nmaslenn@cougarnet.uh.edu)

9 **Abstract.** The grounding line, delineating the boundary where a grounded glacier goes afloat in ocean water, shifts in  
10 response to tidal cycles. Here we analyze COSMO-SkyMed Differential Interferometric Synthetic Aperture Radar  
11 data acquired in 2020 and 2021 over Totten, Moscow University, and Rennick glaciers in East Antarctica, detecting  
12 tide-induced grounding line position variations from 0.5 to 12.5 km along prograde slopes ranging from ~0 to 5%.  
13 Considering a glacier as a non-Newtonian fluid, we provide two-dimensional formulations of the viscous and  
14 viscoelastic short-term behavior of a glacier in partial frictional contact with the bedrock, and partially floating on sea  
15 water. Since the models' equations are not amenable to analytical treatment, numerical solutions are obtained using  
16 FEniCS, an open-source Python package. We establish the dependence of the grounding zone width on glacier  
17 thickness, bed slope, and glacier flow speed. The predictions of the viscoelastic model match ~93% of all the DInSAR  
18 grounding zone measurements and are ~71% more accurate than those of the viscous model. The results of this study  
19 underscore the critical role played by ice elasticity in continuum mechanics-based glacier models, and being validated  
20 with the DInSAR measurements, can be used in other studies on glaciers.

## 21 1. Introduction

22 The grounding line, which defines the boundary between the ice sheet (the portion of a glacier laying on the bedrock)  
23 and the ice shelf (the portion floating on the ocean water), is of particular significance for comprehensive Antarctic  
24 investigations (Friedl et al., 2020; Haseloff and Sergienko, 2018; Schoof, 2007a). The grounding line is a crucial  
25 indicator of glacier stability, as its position reflects the salient glacier dynamics and influences the overall glacier force  
26 and mass balances (Davis et al., 2023; Davison et al., 2023; Holland, 2008; Marsh et al., 2016). Grounding lines not  
27 only provide valuable information about glacier stability by enabling the evaluation of ice thickness, but also allow  
28 the monitoring of sea level changes due to climate warming (Schoof, 2007a; Goldstein et al., 1993; Friedl et al., 2020).  
29 The mechanism governing variations in grounding line position is complex and involves both long-term and short-  
30 term processes (Sergienko, 2022; Sergienko and Haseloff, 2023). Here we focus on short-term grounding line  
31 migrations induced by tidal forces and occurring within a tidal cycle (Coleman et al., 2002; Dempsey et al., 2021;  
32 Albrecht et al., 2006; Freer et al., 2023; Beldon and Mitchell, 2010; Warburton et al., 2020). Differential  
33 Interferometric Synthetic Aperture Radar (DInSAR) and altimeter techniques applied across various Antarctic glaciers  
34 have shown that the magnitude of tide-induced grounding line migrations can extend to several kilometers; several  
35 orders of magnitude wider than the grounding zone width expected from hydrostatic equilibrium (Brancato et al.,



36 2020; Freer et al., 2023; Minchew et al., 2017; Begeman et al., 2020; Milillo et al., 2022; Dawson and Bamber, 2017;  
37 Brunt et al., 2010). Long-term glacier models primarily aim to estimate grounding line evolution over time scales  
38 significantly exceeding tidal scales, thus neglecting short-term variations (Thomas and Bentley, 1978; MacAyeal,  
39 1989; Schoof, 2007b; Weertman, 1974; Gudmundsson et al., 2012; Durand et al., 2009b, a; Cornford et al., 2020;  
40 Favier et al., 2014; Gagliardini et al., 2016; Pattyn et al., 2012; Seroussi et al., 2014; Muszynski and Birchfield, 1987;  
41 Pegler and Worster, 2013; Pegler et al., 2013; Robison et al., 2010). Conversely, short-term glacier models focus on  
42 tidal time scales and tend to disregard the long-term evolution of glaciers due to its negligible impact over these shorter  
43 periods (Rosier et al., 2014; Rosier and Gudmundsson, 2020; Stubblefield et al., 2021).

44 Short-term glacier dynamics has been studied using different physical approaches (Warburton et al., 2020;  
45 Sayag and Worster, 2013, 2011; Tsai and Gudmundsson, 2015; Rosier and Gudmundsson, 2020; Rosier et al., 2014;  
46 Stubblefield et al., 2021). The goal is to quantify the grounding zone width, or the amplitude of the tide-induced  
47 grounding line migrations, by calculating the difference between the grounding line positions at high and low tides  
48 (Ciraci et al., 2023; Gadi et al., 2023; Milillo et al., 2017, 2022; Chen et al., 2023a). For example, a hydrological  
49 model proposed by (Warburton et al., 2020) defines the grounding zone width as the penetration depth into a subglacial  
50 cavity of water interacting with an elastic ice beam that responds to the ocean tides. Several models consider a glacier  
51 as a solid beam moving in a vertical direction due to the periodic tidal impact (Sayag & Worster, 2011, 2013, Tsai &  
52 Gudmundsson, 2015, Chen et al., 2023). In (Sayag and Worster, 2013, 2011) a grounding line migration is considered  
53 a result of the tidal force-induced deformation of an (elastic) Euler-Bernoulli beam. However, they treat the Young's  
54 modulus of ice as a tidal phase-dependent model parameter to support the sustainability of the beam model in fitting  
55 the satellite observations (Sayag & Worster 2013). (Tsai and Gudmundsson, 2015) consider grounding zones as an  
56 opening and closing crack between an elastic ice beam and the bedrock, using equations governing the propagation of  
57 a water-filled crack under pressure. This model, which cannot predict grounding line migrations at low tides, was  
58 modified and applied to the Amery Ice Shelf in Antarctica by (Chen et al., 2023b), who showed that the crack model  
59 can reproduce a kilometer grounding line retreat over a tidal cycle. Nevertheless, the crack-based method is one-  
60 dimensional, as it takes into account only the glacier motion along the ice-bedrock surface and does not describe  
61 motion-induced changes inside the ice. Other models treat glacier ice as a viscous or viscoelastic fluid and seek to  
62 determine grounding line migration by resolving contact forces at the base (Rosier and Gudmundsson, 2020; Rosier  
63 et al., 2014; Stubblefield et al., 2021). (Rosier et al., 2014) and (Rosier and Gudmundsson, 2020) designed nonlinear  
64 viscoelastic models on tidal time scales, where the normal stress and velocity determine the grounding line position  
65 but being considered after discretization, they are not included into the variational formulation used. This technical  
66 detail was addressed by (Stubblefield et al., 2021), who used the full Stokes equations for purely viscous flow and  
67 included contact conditions in the variational formulation.

68 DInSAR data acquired between 2020 and 2021 for Totten, Moscow University, and Rennick glaciers, located  
69 in East Antarctica, show tidally induced grounding zone width values in the kilometer range, which exceed those  
70 estimated from hydrostatic equilibrium by at least one order of magnitude (Brancato et al., 2020; Freer et al., 2023;  
71 Milillo et al., 2022). To model these observations, we present a framework that accurately predicts the temporal  
72 evolution of the grounding line using a continuum mechanics-based approach. We extend the viscous model, proposed



73 by (Stubblefield et al., 2021), by incorporating an elastic component within the framework of the upper-convected  
74 Maxwell model (Snoeijer et al., 2020; Gudmundsson, 2011). The formulation involves variational inequalities  
75 associated with the bedrock boundary conditions for water pressure, ice velocity and normal stress. The variational  
76 inequalities are transformed into variational equalities via a penalty method. Grounding line migrations are obtained  
77 by solving these variational equations at each model timestep using the Finite Element Method (FEM) in the open-  
78 source FEniCS package (Alnæs et al., 2015; Logg et al., 2012). Glacier thickness, bedrock slope, and ice flow serve  
79 as model inputs, and were set based on those for Totten, Moscow University, and Rennick glaciers using Bed Machine  
80 (Morlighem et al., 2017) and Measures InSAR Version 2 (Rignot et al., 2017). Performing the comparison of  
81 automatically generated grounding zones with the grounding zone width values, manually assessed from the DInSAR  
82 interferograms, we evaluate both models' performance and assess the significance of the elastic component relative to  
83 the formulation that accounts for only viscosity. Additionally, we determine the impact the ice-bed system's main  
84 parameters, namely, bedrock slope, glacier thickness, and ice velocity, on the magnitude of tidally induced grounding  
85 line migrations.

## 86 **2. Data and Methods**

87 We assess the models' performance using grounding zone, glacier thickness, bedrock slope, and ice flow velocity  
88 values that characterize Rennick (REN), Moscow University (MU), and Totten (TOT) glaciers (Figure 1). MU and  
89 TOT are neighboring glaciers, located on the Sabrina Coast in East Antarctica (Orsi and Webb, 2022; Fernandez et  
90 al., 2018; Bensi et al., 2022). Together, the combined effect of these two glaciers may result in to up to a 5-meter sea  
91 level rise, making them major contributors to sea level changes in East Antarctica (Mohajerani et al., 2018). Being  
92 characterized by the highest outflow and thinning rate in East Antarctica, TOT also has the third-largest ice flux among  
93 all Antarctic glaciers, following Pine Island and Thwaites glaciers (Roberts et al., 2018; Rignot and Thomas, 2002;  
94 Pritchard et al., 2009). In contrast, MU exhibits relatively slow thinning rates (Mohajerani et al., 2018) and nearly half  
95 the basal melt rate of TOT:  $4.7 \pm 0.8$  m/yr vs  $10.5 \pm 0.7$  m/yr between 2003 and 2008, respectively (Rignot et al.,  
96 2013). Both glaciers are grounded below the sea level, making them potentially unstable and susceptible to collapse  
97 (Van Achter et al., 2022; Aitken et al., 2016). REN, situated in Northern Victoria Land in East Antarctica, spans over  
98 400 km along the flow and narrows from 80 km to 25 km across the flow (Mayewski et al., 1979; Meneghel et al.,  
99 1999; Sturm and Carryer, 1970; Allen et al., 1985). Containing the sea-level equivalent of 11 cm in a form of ice,  
100 REN is also grounded below the sea level and is experiencing rapid thinning due to intensive basal melt (Pritchard et  
101 al., 2012; Rignot et al., 2019). REN's ice discharge has shown up to 20% amplification between 1999 and 2018 (Miles  
102 et al., 2022). Despite exhibiting similar behavior to TOT and MU, REN retreats slower than most Antarctic glaciers,  
103 rendering it relatively stable (Miles et al., 2022; Pritchard et al., 2012).

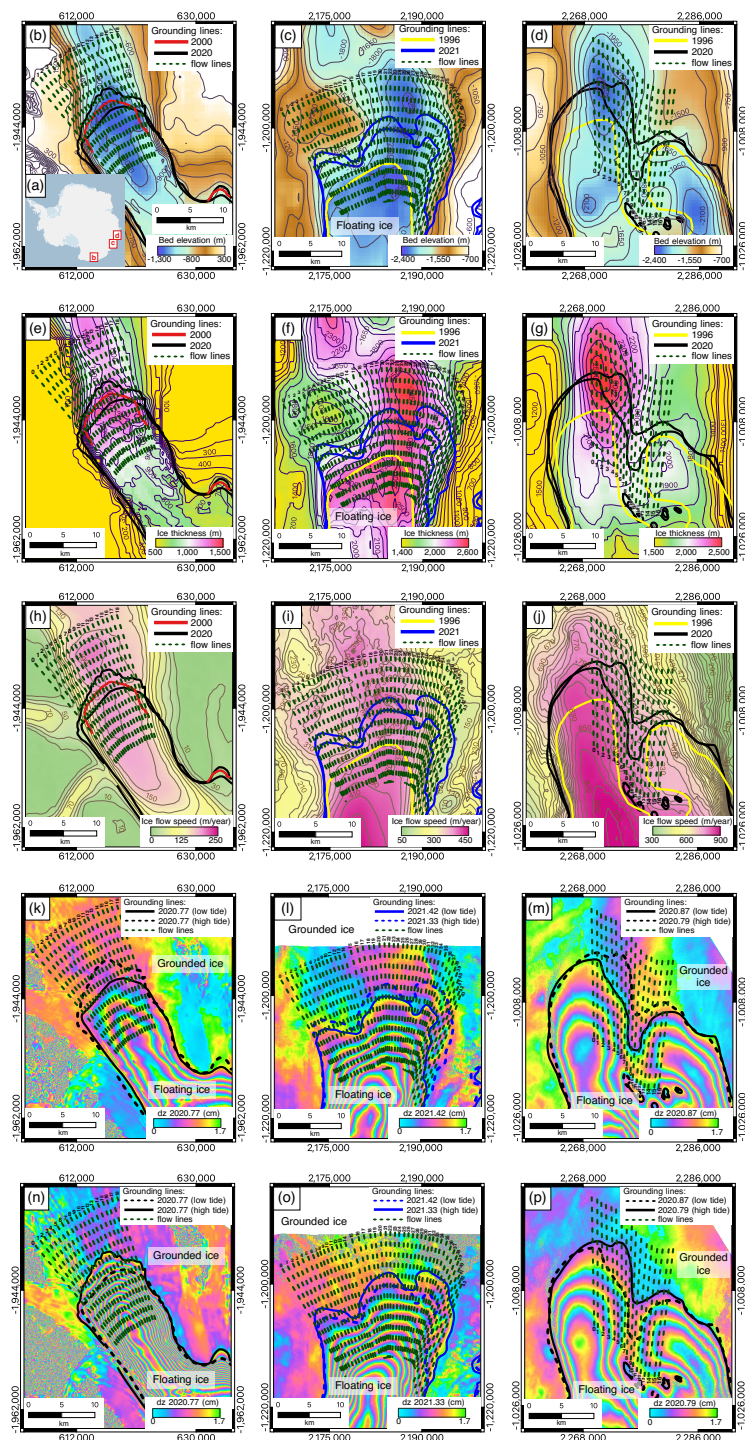
104 We obtain the grounding zone width values for TOT, MU, and REN utilizing a series of 1-day repeat pass Synthetic  
105 Aperture Radar (SAR) data from the COSMO-SkyMed mission, which comprises a four-satellites constellation  
106 equipped with synthetic aperture radars operating at X-band with a wavelength of 3.1 cm (Milillo et al., 2014). Each  
107 of the four satellites has a 16-day repeat cycle, while our analysis focuses on the images collected by the second and  
108 third satellites, capturing data over the same area with a 1-day interval.



109 The interferograms were generated from the STRIPMAP mode of the COSMO-SkyMed, using a set of  $4 \times 5$   
110 consecutive overlaying frames with an azimuth and range resolution of 3 meters and a  $40 \times 40$  km swath. To eliminate  
111 the topographic effect, the Copernicus digital elevation models (DEMs) were employed. To co-register the data and  
112 achieve maximum phase coherence we used satellite orbits for coarse co-registration and used a pixel offsets approach  
113 for fine co-registration. A multi-looking factor of 10 in both range and azimuth was used to achieve an interferogram  
114 resolution of 30 m x 30 m. Two one-day interferometric pairs were combined into one double differential  
115 interferogram (DInSAR) to cancel out horizontal deformation due to glacier flow. Each interferometric pair combined  
116 in a DInSAR interferogram was acquired within 1.5 months over the same satellite track in order to minimize  
117 horizontal velocity changes. An interferometric fringe corresponds to half a wavelength of surface displacement,  
118 equivalent to 1.5 cm of satellite line of sight displacement per fringe for X-band or about 1.7 cm when projecting  
119 deformation onto the vertical considering the satellite incidence angle. The grounding line can be manually delineated  
120 as the most inner fringe in the grounded ice side. Therefore, the DInSAR technique provides information about vertical  
121 tide-induced glacier movements and enables grounding line mapping with accuracy of the order of 100 - 200 m  
122 (Rignot et al., 2014).

123 We use three pairs of DInSAR interferograms, acquired between 2020 and 2021, where each pair covers the main  
124 trunk of one of the glaciers of interest and is obtained within a 1.5-month period to ensure that any variations in the  
125 grounding line position occur due to the tidal interaction rather than glacier retreat (Milillo et al., 2022). Combining  
126 two manually mapped grounding lines for each interferogram in a pair, we establish a grounding zone for the  
127 corresponding glacier and measure the grounding zone width along the ice flow directions.

128 To determine the average thickness of the glaciers and their corresponding bed slopes, the BedMachine Antarctica  
129 (version 2) was employed (Morlighem et al., 2017). Additionally, the MEaSURES (version 2) InSAR-based ice  
130 velocity map of Antarctica was utilized in calculating the average ice flow speed (Rignot et al., 2017). All  
131 measurements were performed along a total of 80 velocity flow lines, located 500 m to 600 m apart, each  
132 approximately 20 km in length, a parameter adopted as the glacier domain length during the modeling process.





134 **Figure 1.** Study area: (a) location of Totten (TOT), Moscow University (MU), and Rennick (REN) glaciers in  
 135 Antarctica. Subplots (b), (c), (d) show the bed elevation relief from BedMachine2 (Morlighem et al., 2017) with 50 m  
 136 contour levels (purple) over REN, MU, and TOT, respectively. Subplots (e), (f), (g) show the ice thickness map with  
 137 100 m contour levels (purple) from BedMachine2 (Morlighem et al., 2017) over REN, MU, and TOT, respectively.  
 138 Subplots (h), (i), (j) show the ice flow velocity map with 20 m/year contour levels (purple) from MEaSURES2 (Rignot  
 139 et al., 2017) over REN, MU, and TOT, respectively. Subplots (k), (l), (m) show the DInSAR interferogram at low tide  
 140 with a corresponding grounding line as a solid line and a grounding line at high tide as a dashed line over REN, MU,  
 141 and TOT, respectively. Subplots (n), (o), (p) show the DInSAR interferogram at high tide with a corresponding  
 142 grounding line as a solid line and a grounding line at low tide as a dashed line over REN, MU, and TOT, respectively.  
 143 The grounding lines over REN and TOT were mapped in 2020 (black line), while the grounding lines over MU (blue  
 144 line) correspond to 2021. The grounding lines for 1996 (yellow line) and 2000 (red line) on figures (b) – (j) were taken  
 145 from MEaSURES2 DInSAR-based Antarctic grounding line dataset (Rignot et al., 2016). Numbered dark green dotted  
 146 lines represent the flow lines, along which the measurements (Table S1) were performed. All datasets are represented  
 147 in Antarctic projection (EPSG:3031).

### 148 3. Viscous and viscoelastic models

149 The short-term grounding line migration model, rooted in the Navier-Stokes equations under the assumption of  
 150 viscoelastic ice flow, is based on the purely viscous formulation of the same problem (Stubblefield et al., 2021). Here  
 151 we summarize the similarities and differences between the models, while the comprehensive description of the  
 152 viscoelastic model including the derivation of the model’s penalized problem (A35), and the details about the models  
 153 comparison are provided in Appendix A: Glacier modelling.

154 For both models, we designate the glacier domain as  $\Omega$ , as shown in Figure 2, with a piece-wise smooth boundary  $\partial\Omega$ .  
 155 We place the glacier in the two-dimensional coordinate system  $(X, Y)$ , where  $X$  denotes the horizontal axis, and  $Y$  is  
 156 used for identifying the vertical axis. In the principal notation used in this paper, a spatial point is denoted by  $\mathbf{x} =$   
 157  $(x, y) \in \bar{\Omega}$ , where an overline denotes the set closure. For glacier length  $L$ , the ice domain  $\Omega$  can be mathematically  
 158 expressed as

$$\Omega = \left\{ (x, y): |x| < \frac{L}{2}, s(x, t) < y < h(x, t) \right\} \quad (1)$$

159 The glacier boundary is represented as a union of five complementary parts:

$$\partial\Omega = \Gamma_D \cup \Gamma_N \cup \Gamma_w \cup \Gamma_b \cup \Gamma_a, \quad (2)$$

160 where  $\Gamma_D$  is an inflow boundary,  $\Gamma_N$  is an outflow boundary,  $\Gamma_w$  is an ice–water surface,  $\Gamma_b$  is an ice–bedrock surface,  
 161 and  $\Gamma_a$  is an ice–air surface. Defining  $f(x)$  as a bedrock slope function,  $h(x, t)$  as a time-dependent function of the  
 162 glacier surface elevation, and  $s(x, t)$  as a function, defining the position of lower boundary of the ice shelf with time,  
 163 the ice–water and ice–bed boundaries are expressed as

$$\Gamma_w = \{(x, y) \in \partial\Omega: y = s(x, t) > f(x)\}, \quad (3)$$

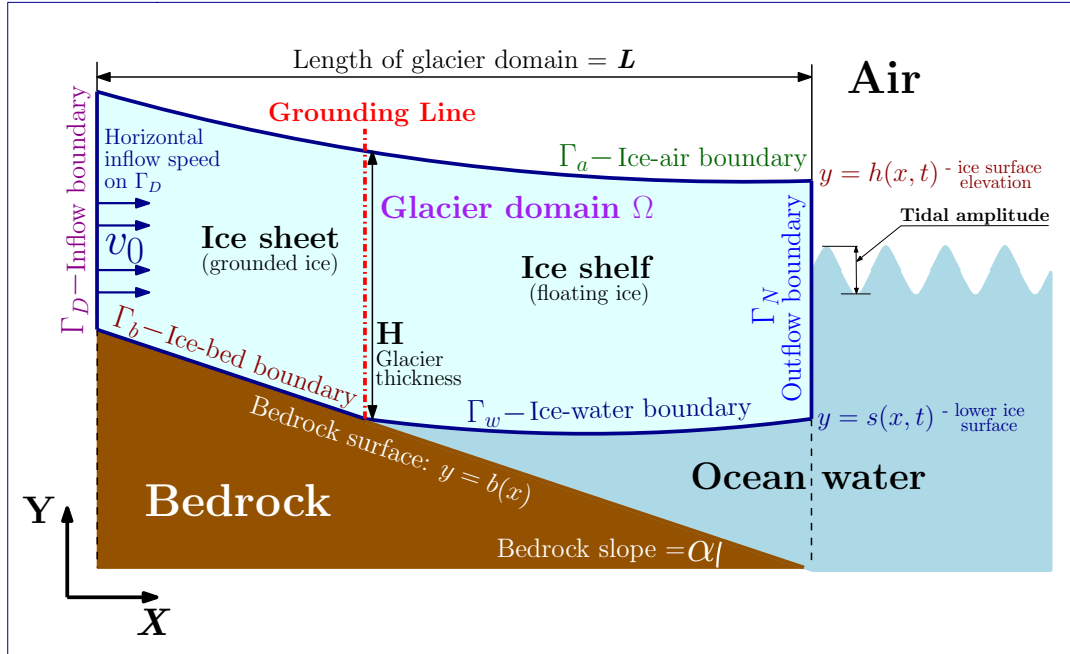
$$\Gamma_b = \{(x, y) \in \partial\Omega: y = s(x, t) = f(x)\}. \quad (4)$$

164 The entire lower boundary  $\Gamma_s$  therefore, is identified as a union of the ice–water and ice–bed boundaries:



$$\Gamma_s = \Gamma_w \cup \Gamma_b = \{(x, y) \in \partial\Omega: y = s(x, t) \geq f(x)\} \quad (5)$$

165 The grounding line position is identified as a point, where the ice–water boundary intersects the ice–bed boundary.



166

167 **Figure 2.** Model geometry for both viscous and viscoelastic problems, highlighting the ice domain  $\Omega$  boundaries, as  
168 defined in Table A1.

169 The bedrock slope in the models is set using the function

$$b(x) = -\frac{Ax}{L}, \quad (6)$$

170 Where  $A$  is a variable parameter in meters that determines the bedrock inclination, and  $L$  is a glacier domain length,  
171 which is kept constant at 20 km for all model runs to ensure consistent results. The bed slope  $\alpha$  is determined as the  
172 tangent of the bedrock function  $b(x)$  and is measured

$$\alpha = \frac{A \cdot 100\%}{L}. \quad (7)$$

173 Both viscous and viscoelastic models require bed slope, glacier thickness and ice inflow speed as input parameters.  
174 For one set of input parameters, the code solves the corresponding variational problem twice: first, for a calm ocean  
175 surface without tides to stabilize the glacier and approximate its shape to a more natural geometry than the initially  
176 specified one; and second, for the tidal situation where the grounding zone width is determined. We employ sinusoidal-  
177 shaped tides with a 1 m amplitude and a half-day period  $P$ , which is typical for the investigated glaciers (Padman et  
178 al., 2018; Hibbins et al., 2010). Thus, the sea level in a tidal case changes with time as

$$l(t) = \frac{\rho_i}{\rho_w} H + \sin\left(\frac{2\pi t}{P}\right), \quad (8)$$

179 where  $H$  is the glacier thickness at the grounding line.



180 The grounding line position is defined based on the numerical tolerance  $\xi$ , set to 1 mm. If the computed position of a  
 181 lower boundary mesh node  $s$  is  $\xi$  mm greater in the vertical direction than the bedrock, that node is classified as  
 182 floating. Conversely, if a node position does not deviate from the bed by more than  $\xi$ , that node is classified as  
 183 grounded. Schematically, the node classification can be described as:

$$\begin{cases} s - b \leq \xi \Rightarrow \text{grounded node} \\ s - b > \xi \Rightarrow \text{floating node} \end{cases} \quad (9)$$

184 Both models consider a glacier as an incompressible and non-Newtonian ice flow, sharing the same domain and  
 185 restricted by identical boundary conditions. Using FEniCS, a freely available FEM Python package, the models  
 186 employ Taylor–Hood elements for velocity and pressure fields to solve a corresponding variational problem on each  
 187 time step by means of a Newton solver for nonlinear systems of equations. The primary distinction between the viscous  
 188 and viscoelastic models lies in the incorporation of an elastic component, represented by Hooke’s law. While the  
 189 addition of the elastic component enables the viscoelastic model to account for significant short-term glacier  
 190 deformations, as provided by the application of the upper-convected Maxwell model of viscoelasticity (see  
 191 A2.1. Governing equations), it also entails a substantial increase in computational resources required for a single  
 192 model run. A comparative analysis of the main parameters of the models is presented in Table 1. The detailed  
 193 exposition of the viscoelastic model is provided in Appendix A: Glacier modeling, while the main specifications of  
 194 the viscous model can be found in (Stubblefield et al., 2021).

195 **Table 1.** Comparison of the main properties of the viscous and viscoelastic models.

Characteristics	Viscous model	Viscoelastic model	Similarity	
<b>Material properties of glacier flow</b>				
Compressibility	Incompressible	Incompressible	Same	
Rheological behavior	Non-Newtonian	Non-Newtonian	Same	
Material behavior	Viscous	Viscoelastic	Different	
<b>Physical formulation of the models</b>				
Glacier domain	Equations (1) – (5)	Equations (1) – (5)	Same	
Boundary conditions	Equations (A17) – (A22)	Equations (A17) – (A22)	Same	
Governing equation	Conservation of mass in case of incompressibility	Equation (A1)	Equation (A1)	Same
	Conservation of momentum (Stokes equation)	Equation (A2)	Equation (A2)	Same
	Constitutive law (Hooke’s law)	Both Hooke’s law (A3) and ice viscosity (A5) are defined via strain rate tensor (A4)	Both Hooke’s law (A6) and ice viscosity (A8) are defined via deviatoric stress tensor $\tau$ (A7), which, in turn, depends on strain rate tensor (A4)	Different
<b>Implementation of the models</b>				
Penalized problem solved by the model on each time step	Equation (3.21) in (Stubblefield et al., 2021)	Equation (A35)	Different	





Computation time* (HH:MM:SS)	Glacier thickness = 1.0 km	01:07:07	02:57:48	Different
	Glacier thickness = 1.5 km	01:34:29	04:21:10	Different
	Glacier thickness = 2.0 km	01:59:54	06:07:50	Different
	Glacier thickness = 2.5 km	02:41:39	07:30:08	Different

\* For 2.3 GHz 8-Core Intel Core i9 processor. Model input parameters: Domain length = 20 km; Bed slope = 1.0 %; Inflow speed = 100 m/year; Mesh size = 250 m and 50 m on upper and lower domain boundaries, respectively. The time is provided the HH:MM:SS format, where H shows the number of hours, M shows the number of minutes, and S is the number of seconds

196 **4. Results**

197 A total of 80 flow lines were utilized for computing ice-bed system parameters, namely, grounding zone width, ice  
 198 thickness, bed slope, and ice flow speed at the grounding zone. All measured parameters are listed in Table S1, while  
 199 a statistical summary of these measurements is provided in Table 2. The three glaciers rest on prograde bedrock slopes,  
 200 gradually ascending inland. TOT exhibits the shallowest average bed slope among the glaciers of interest, measuring  
 201  $1.1 \pm 0.1$  %. The glacier has average grounding zone width of  $4.0 \pm 0.4$  km and a mean thickness of  $2.1 \pm 0.1$  km,  
 202 making it the fastest one among the three glaciers with an average speed of  $691 \pm 77$  m/year. In contrast, REN is the  
 203 thinnest and slowest among the three, with a mean thickness of  $1.0 \pm 0.2$  km and a flow speed of  $170 \pm 16$  m/year. It  
 204 also features the smallest average grounding zone width of  $2.3 \pm 0.4$  km and a rising inland bed with an average rate  
 205 of  $1.2 \pm 0.1$  %. MU, characterized by the largest mean grounding zone of  $4.9 \pm 0.4$  km, also has the steepest average  
 206 bed slope of  $1.4 \pm 0.2$  %. With an average thickness of  $2.2 \pm 0.1$  km, the glacier maintains a mean ice flow speed of  
 207  $239 \pm 26$  %.

208 **Table 2.** Minimum, maximum, and average values of the grounding zone width, ice thicknesses, bed slopes, and ice  
 209 flow speed of Totten (TOT), Moscow University (MU), and Rennick (REN) glaciers.

Glacier characteristics		TOT	MU	REN	Data source
<b>Grounding zone, km</b>	Min	$0.9 \pm 0.4$	$0.4 \pm 0.4$	$0.8 \pm 0.4$	Pairs of DInSAR interferograms
	Mean	$4.0 \pm 0.4$	$4.9 \pm 0.4$	$2.3 \pm 0.4$	
	Max	$7.6 \pm 0.4$	$12.5 \pm 0.4$	$3.3 \pm 0.4$	
<b>Ice thickness, km</b>	Min	$1.8 \pm 0.2$	$1.7 \pm 0.1$	$0.7 \pm 0.4$	BedMachine2 (Morlighem et al., 2017)
	Mean	$2.1 \pm 0.1$	$2.2 \pm 0.1$	$1.0 \pm 0.2$	
	Max	$2.4 \pm 0.1$	$2.4 \pm 0.2$	$1.2 \pm 0.1$	
<b>Bed slope, %</b>	Min	$0.02 \pm 0.02$	$0.01 \pm 0.01$	$0.3 \pm 0.1$	BedMachine2 (Morlighem et al., 2017)
	Mean	$1.1 \pm 0.1$	$1.4 \pm 0.2$	$1.2 \pm 0.1$	
	Max	$4.6 \pm 0.2$	$5.4 \pm 0.3$	$5.2 \pm 0.2$	
<b>Ice flow speed, m / year</b>	Min	$547 \pm 103$	$149 \pm 31$	$113 \pm 58$	MEaSURES2 (Rignot et al., 2017).
	Mean	$691 \pm 77$	$239 \pm 26$	$170 \pm 16$	
	Max	$758 \pm 55$	$378 \pm 12$	$188 \pm 7$	



211 As both models necessitate the specification of bed slope, ice inflow speed, and glacier thickness prior to execution,  
212 we conceptually represent the set of input parameters as (model, slope, thickness, speed), where ‘model’ denotes either  
213 the viscous or viscoelastic formulation. Table 2 shows that for the considered glaciers, ice thickness ranges from  
214  $0.7\pm 0.4$  km to  $2.4\pm 0.2$  km, bed slope varies from  $0.01\pm 0.01\%$  to  $5.4\pm 0.3\%$ , and ice flow speed can be as low  
215 as  $113\pm 58$  m / year and as high as  $758\pm 55$  m / year. Therefore, taking the bed slope in a range from 5% to 0.05%,  
216 glacier thickness in a range from 1.0 to 2.5 km, and ice inflow speed in a range from 100 to 800 m/year, we ensure  
217 that ~95% of the measurements align with the model setup (see Table S1).

218 Once the range of input parameters was established, we examined the sensitivity of the models to mesh size by running  
219 them with the same set of parameters but varying mesh sizes at the lower domain surface (from 10 m to 250 m with  
220 10 m step), while keeping the mesh size constant (250 m) at the upper surface of the glacier. Overall, to establish the  
221 most efficient mesh size, 200 grounding zone width values were obtained and analyzed (Figure S1). The accuracy of  
222 the viscoelastic model is more significantly affected by mesh size than the viscous model. For example, grounding  
223 zone width values for glaciers with thicknesses of 2.5 km and 1 km, both with an inflow speed of 100 m/year, converge  
224 to approximately 1.45 km for a mesh size of 250 m. However, at a mesh size of 10 m, these values were 0.96 km and  
225 0.84 km, respectively (Figure S1 (d)). Comparing the dependences for the same slope of 5% for both models, we  
226 conclude that for glaciers with the same thickness, lower ice flow speed is more sensitive to the mesh size (red and  
227 black dots in Figure S1 (c) and (d)).

228 We empirically determined that the average accuracy of manual mapping is approximately 200 m, therefore as long  
229 as the model outputs do not deviate by more than 0.2 km from the asymptotic value of the grounding zone width, we  
230 can conclude that the mesh impact lies within the confidence interval of manual mapping. The noticeable accuracy  
231 deterioration, exceeding 200 m, occurs at a mesh size of 210 m for the viscous model (Figure S1 (a)), and 200 m for  
232 the viscoelastic model (Figure S1 (d)). However, for the viscoelastic model, we observe several step-like changes in  
233 the grounding zone width value, with the first noticeable shift taking place occurring at a mesh size of 60 m (Figure S1 (b)).  
234 Therefore, to ensure the greatest possible modelling precision and maintain the consistency of the results, we have  
235 chosen 50 m as the mesh size at the lower domain boundary for the following main analysis.

236 The main analysis of the grounding zone evolution depending on physical representation (viscous or viscoelastic) and  
237 ice-bed system parameters was carried out retaining a constant mesh size of 50 m and 250 m at the lower and upper  
238 domain boundaries, respectively, which was previously determined as the most efficient. Maintaining a consistent  
239 glacier domain length of 20 km for all model runs, various parameter tests were conducted, encompassing ice  
240 thicknesses of 1.0, 1.5, 2.0, and 2.5 km; horizontal ice inflow speeds of 100, 350, 600, and 800 m/year; and bedrock  
241 slopes of 5.0, 4.5, 4.0, 3.5, 3.0, 2.5, 2.0, 1.5, 1.0, 0.5, 0.1, and 0.05% (see Figure S2). Therefore, a total of 192 sets of  
242 initial parameters were investigated for each model, covering all possible combinations of the specified ice thickness,  
243 ice inflow speed, and bedrock slope values. For each parameter set, both the viscous and viscoelastic models were  
244 initially run for a duration of two months within the model's time frame, assuming a stationary ocean with no tides to  
245 allow the model to reach stability. Subsequently, the models were run over a 7-day period with tides incorporated. In  
246 the still water scenario, the water level corresponds to the low tide situation in the tidal problem. The choice of a one-  
247 week time limit for the tidal problem allows the model to adapt to tidal impacts and enhances results accuracy. In most



248 tidal model runs, the grounding zone width slightly increases within the first 3 to 5 days with each tide while the  
249 models adapt and stabilizes afterward. The resulting grounding zone width value for each model run is determined as  
250 the average of the grounding zone width values for the last two days.

251 The source code of the viscous model, developed by (Stubblefield et al., 2021), was used as a basis of the viscoelastic  
252 model (see Code and Data availability). Necessary adjustments to the mesh size and glacier parameters for both  
253 publicly available source codes were made accordingly. Consequently, a total of 1,168 model runs were performed  
254 while conducting the research: 400 runs for the mesh sensitivity analysis and 768 runs for the main analysis, which  
255 includes the grounding zone width dependence analysis from the main glacier parameters for both models. As for the  
256 grounding line generation two model runs are required, 584 grounding zone values were obtained: 200 for the mesh  
257 sensitivity analysis and 384 for the main analysis. In total, these code runs required about 1400 hours (~58 days) of  
258 continuous computations.

## 259 5. Discussion

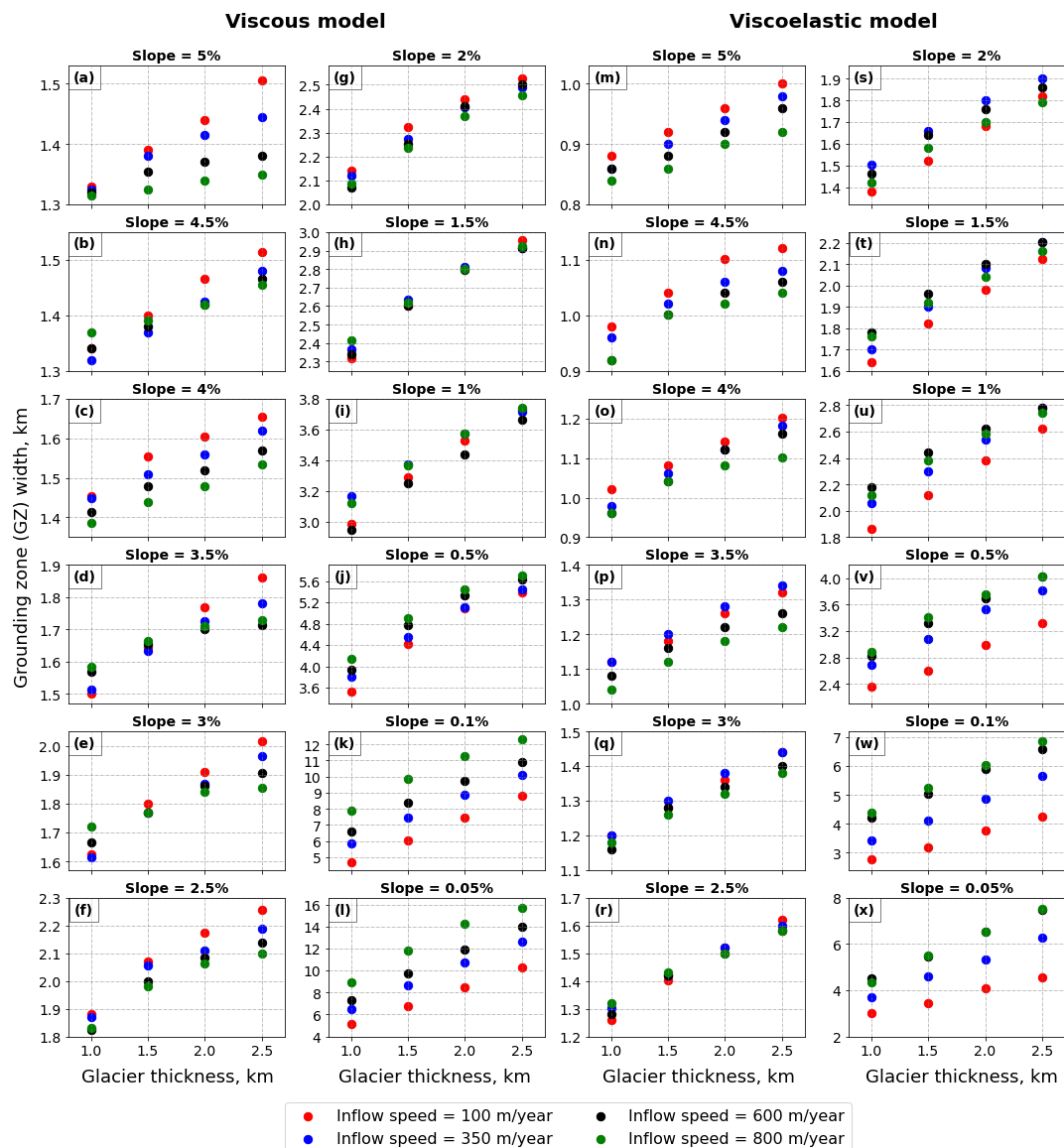
### 260 5.1. Modeled tide-induced grounding zone dependence from ice-bed system parameters

261 A total of 384 grounding zone width values were generated utilizing all possible combinations of selected ice-bed  
262 system parameters (Figure S2), while maintaining constant mesh sizes of 250 m and 50 m at the upper and lower  
263 glacier surfaces, respectively. These grounding zones are illustrated in Figure 3, where they are grouped by the bedrock  
264 slope for each model. Figure 3 shows the dependence of the grounding zone width on the glacier thickness for each  
265 bed slope, with the outputs color-coded based on the inflow speed. The relationship between modeled grounding zone  
266 width ( $GZ$ ) and ice thickness ( $H$ ) for each inflow speed and bed slope can be approximated by a linear function  $GZ =$   
267  $a \cdot H + b$ , where coefficients  $a$  and  $b$  are unique for each model formulation, bed slope, and ice inflow speed. The  
268 approximation equations with corresponding coefficients of determination ( $R^2$  values) are provided in Table S2,  
269 where  $R^2$  ranges from 0.902 to 1.000 for the viscous model and from 0.874 to 1.000 for the viscoelastic model,  
270 showing a high linearity of the grounding zone dependence on the glacier thickness for any bedrock slope if ice speed  
271 is constant.

272 The linear approximation  $GZ = a \cdot H + b$  of the values shown in Figure 3, performed separately based on the bed  
273 slope for each inflow speed, facilitates tracking the evolution of the grounding zone dependence on ice flow speed as  
274 the bed slope increases. Denoting  $a_{100}$ ,  $a_{350}$ ,  $a_{600}$ ,  $a_{800}$  as slope coefficients for ice inflow speeds of 100, 350, 600,  
275 and 800 m/year, respectively, reveals the following evolution of their relative magnitudes:  $a_{100} > a_{350} > a_{600} > a_{800}$   
276 for bed slope  $5.0\% \geq \alpha \geq 3.0\%$  and  $\alpha = 0.5\%$ ,  $a_{100} > a_{600} > a_{350} > a_{800}$  for bed slope  $2.5\% \geq \alpha \geq 1.5\%$ ,  
277  $a_{600} > a_{100} > a_{800} > a_{350}$  for bed slope  $\alpha = 1.0\%$ ,  $a_{350} > a_{100} > a_{600} > a_{800}$  for bed slope  $\alpha = 0.1\%$ , and  
278  $a_{800} > a_{600} > a_{350} > a_{100}$  for bed slope  $\alpha = 0.05\%$  for the viscous model (see Table S2 and Figure 3). Analogously,  
279 for the viscoelastic model, the slope coefficients demonstrate the following pattern:  $a_{100} > a_{350} \geq a_{600} > a_{800}$  for  
280 bed slope  $5.0\% \geq \alpha \geq 4.5\%$  and  $2.5\% \geq \alpha \geq 2.0\%$ ,  $a_{350} > a_{100} > a_{600} \geq a_{800}$  for bed slope  $4.0\% \geq \alpha \geq 3.5\%$   
281 and  $\alpha = 1.5\%$ ,  $a_{100} > a_{600} > a_{350} > a_{800}$  for bed slope  $\alpha = 3.0\%$ ,  $a_{100} > a_{350} > a_{800} > a_{600}$  for bed slope  $\alpha =$   
282  $1.0\%$ ,  $a_{600} > a_{350} > a_{800} > a_{100}$  for bed slope  $\alpha = 0.5\%$ ,  $a_{800} > a_{600} > a_{350} > a_{100}$  for bed slope  $0.1\% \geq \alpha \geq$   
283  $0.05\%$ . Therefore, at steeper slopes, both models exhibit the same ratio of slope coefficients, namely,  $a_{100} > a_{600} >$



284  $a_{350} > a_{800}$ , which changes to the reverse ratio at shallower slopes:  $a_{800} > a_{600} > a_{350} > a_{100}$ . This indicates that  
 285 at steeper slopes, a grounding zone is more sensitive to changes in glacier thickness if the ice flow is slow, while for  
 286 almost flat bedrocks, a grounding zone width is more affected by variations in ice thickness of faster-flowing glaciers.



287

288 **Figure 3.** Dependence of the grounding zone width from the glacier thickness for all considered inflow speeds and  
 289 bed slopes for both viscous and viscoelastic models. Subplots (a) – (l) correspond to the viscous model; subplots  
 290 (m) – (x) correspond to the viscoelastic model. Corresponding bed slope is written above each subplot, the x-axis of  
 291 each subplot shows the glacier thickness in meters, while the y-axis shows the evolution of the grounding zone as the



292 glacier becomes thicker. Each subplot contains four sets of values, colored based on the inflow speed used as a model  
293 input at a corresponding model run.

294 Additionally, Figure 3 and Table S2 also show that the linear dependence  $GZ = a \cdot H + b$  becomes steeper as the bed  
295 slope decreases, which, in terms the slope coefficient  $a$ , means that the coefficient's magnitude increases as the  
296 bedrock becomes shallower. We conducted further analysis using the data from Figure 3 by subtracting the grounding  
297 zone widths corresponding to the thickest and the thinnest glaciers ( $\Delta GZ$ ) for each bed slope and ice flow speed. While  
298 this analysis aimed to assess the impact of glacier thickness on the grounding zone for different bed slopes, Table S3  
299 confirms the previous conclusion that the grounding zone at steep bed slopes is more sensitive to lower flow speeds,  
300 as evidenced by the descending order of  $\Delta GZ$  values in the column corresponding to 5.0% bed slopes for both models.  
301 Conversely, both models exhibit an ascending order of  $\Delta GZ$  values in 0.05% column, indicating a higher sensitivity  
302 of grounding zone to ice thickness for faster flowing glaciers.

303 The  $\Delta GZ$  values, averaged between those corresponding to different flow speeds for each bed slope and denoted as  
304 'Mean' in Table S3, increase as the bed slope decreases. This pattern is observed for both models, with the mean  
305 difference values being larger for the viscous model. At a 5.0% bed slope, the difference in mean  $\Delta GZ$  does not exceed  
306 10 meters: 98 m versus 105 m for the viscous and viscoelastic models, respectively. The difference in  $\Delta GZ$  remains  
307 similar between 5.0% and 1.0% bed slopes, while  $\Delta GZ$  for the viscoelastic model is less than two times greater than  
308  $\Delta GZ$  for the viscous model. However, at a 0.5% bed slope,  $\Delta GZ$  for the viscous model becomes greater than  $\Delta GZ$  for  
309 the viscoelastic model. At a bed slope of 0.05%,  $\Delta GZ$  for the viscous model is almost 2.4 times greater than that for  
310 the viscoelastic model: 6130 m versus 2543 m for viscous and viscoelastic models, respectively. Moreover, the  
311 viscous model predicts a ~62 times enlargement of  $\Delta GZ$  if the bed slope changes from 5.0% to 0.05%, while the  
312 viscoelastic model forecasts a ~24 times enlargement of  $\Delta GZ$  for the same slope change.

## 313 5.2. Model validation with DInSAR grounding zone measurements

314 In addition to the grounding zone, along each of 80 profiles we calculated the average values of bedrock slope, glacier  
315 thickness, and flow speed. While grounding zones were used to verify the models' performances, bed slopes, ice  
316 thicknesses, and flow speeds were used as input parameters. Therefore, as every profile is characterized by three input  
317 measurements, a total of 240 input measurements were performed. We test the models using bed slopes varying from  
318 5% to 0.05% with ice thicknesses ranging from 1.0 to 2.5 km, and ice inflow speeds from 100 to 800 m/year. This  
319 choice of model input parameters ranges ensures that ~97% of the input measurements, accounting for the  
320 corresponding measurement errors, fall within the specified ranges (Table S1).

321 The relative distribution of input measurements is shown in Figure S3. All the ice flow measurements (Figure S3) fall  
322 between 100 m/year and 800 m/year, with REN's speed measurements being smaller than 200 m/year, MU's values  
323 ranging between 150 and 400 m/year, and TOT's speeds exceeding 500 m/year. REN does not have slopes lower than  
324 0.8%, while MU and TOT have shallower slopes. Histogram (j) in Figure S3 shows high density of measurements  
325 clustered between 0% and 0.2% bedrock slopes if not accounting for the measurement errors. Due to computational  
326 limitations, we are unable to model bedrock slopes shallower than 0.05%. However, considering bed slopes associated  
327 errors (Figure 4), the minimum bed slope of 0.05% ensures that all the measurements along shallow beds fall into the



328 modeled range of bed slopes (from 0.05% to 5%). Three bed slope measurements are greater than 5.0%, with two  
329 belonging to MU (profiles 27 and 28 in Table S1) and one to REN (profile 0). The Interquartile Range (IQR) method  
330 of outlier removal, which classifies a data point as an outlier if it exceeds the 25<sup>th</sup> percentile of the dataset by more  
331 than  $1.5 \cdot IQR$  or falls behind the 75<sup>th</sup> percentile by more than  $1.5 \cdot IQR$ , detected these three measurements as outliers  
332 (empty dots in box plot E1 in Figure S3). Only four thickness measurements, all belonging to REN  
333 (profiles 0, 1, 2, and 3), are less than 1 km (histograms (h) and (k) in Figure S3), and were classified by the IQR-based  
334 method as outliers as well (empty dots in box plot (n) in Figure S3). These seven measurements (four for ice thickness  
335 and three for bed slope), determined by the IQR-based method as outliers belong to six profiles: four for REN (profiles  
336 0, 1, 2, and 3), and two for MU (profiles 27, 28). We assess the models' capabilities to model DInSAR-observed  
337 grounding zones including and excluding these six profiles (Figure 4d).

338 Figure 4 provides the comparison of the viscous and viscoelastic models with each other and with the remote sensing  
339 observations over MU, TOT, and REN glaciers. Figure 4 (a) and Figure 4 (b) present the grounding zone width  
340 obtained for the viscous and viscoelastic models, respectively, where the results for different inflow speeds are  
341 averaged by glacier thickness. Error bars in Figure 4 (a) and Figure 4 (b) represent critical grounding zone width  
342 values, which are dependent on ice speed for a given ice thickness. The grounding zone width for both models  
343 increases as the bedrock slope decreases. The steepest dependence is observed for the smallest tested glacier thickness  
344 (1 km), while the shallowest dependence, resulting in the largest grounding zone width values, characterizes the  
345 thickest glaciers (2.5 km). The grounding zone width values of the viscoelastic model ( $GZ_{VE}$ ) plotted against the  
346 viscous model's outputs  $GZ_V$ , as shown in Figure 4 (d), exhibit a linear relationship:  $GZ_{VE} = 0.49 \cdot GZ_V + 0.47$ , with  
347 a coefficient of determination ( $R^2$ ) of 0.97. Consequently, for any combination of bedrock slope, glacier thickness,  
348 and ice inflow speed, the grounding zone width obtained from the viscoelastic model is nearly half that of the  
349 grounding zone width calculated by the viscous model on shorter time scales.

350 As each profile is characterized by a specific slope, thickness, and speed measurement, the measurements falling  
351 outside the chosen ranges pertain to six profiles: four for REN (profiles 0, 1, 2, and 3), and two for MU (profiles 27  
352 and 28). These profiles are labeled as 'extra' profiles in Table S2. We performed the assessment of the models'  
353 capabilities to replicate DInSAR-observed grounding zones, both including and excluding these 'extra' profiles.  
354 Figure 4 C indicates the superimposed outputs of the viscous and viscoelastic models alongside the DInSAR  
355 grounding zone measurements overlaid on the modeling results, where empty circular markers correspond to the  
356 grounding zones extracted along the 'extra' profiles.

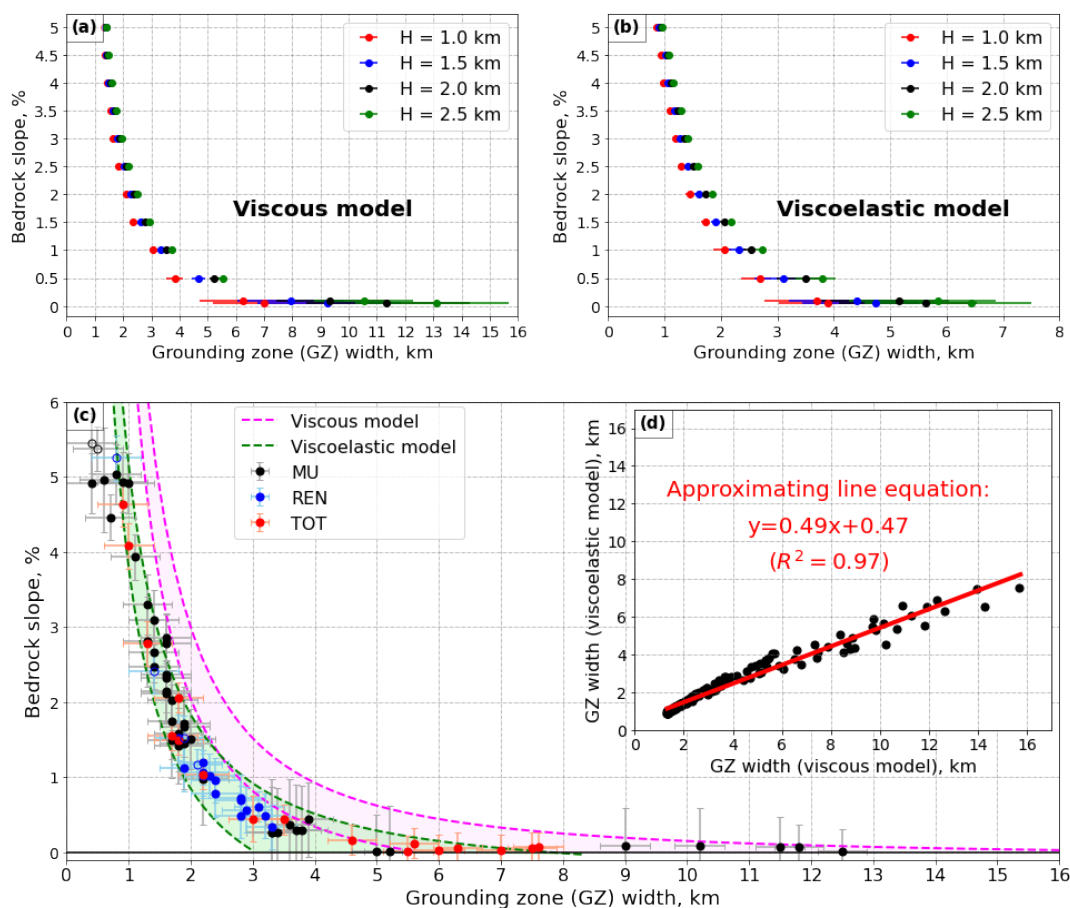
357 Considering all 80 profiles and disregarding the measurements' error bars, ~41%, ~0%, and ~14% of TOT's, REN's,  
358 and MU's measurements, respectively, fall into the viscous model's domain. Meanwhile, ~88% of TOT's  
359 measurements, 100% of REN's measurements, and ~71% of MU's measurements, all without considering the error  
360 bars, are successfully accommodated by the viscoelastic model. When including the error bars in consideration, the  
361 performance of the models significantly improves. For the viscous model, the percentage of successfully modeled  
362 measurements increases from ~41% to ~65% for TOT, from ~0% to ~26% for REN, and from ~14% to ~39% for  
363 REN. For the viscoelastic model, this performance improvement is evident in the following notable expansions: from  
364 ~88% to ~100% for TOT, from ~71% to ~84% for MU and remains consistently at 100% for REN. Excluding the



365 'extra' profiles, ~29% versus ~57% of the TOT's measurements fall within the domain of the viscous model when  
366 disregarding and considering the measurements' error bars, respectively. Analogously, for the viscous model, ~0%  
367 turns into ~33% for REN, and ~13% transforms into ~47% for MU when taking the measurements' error bars into  
368 account. Disregarding the 'extra' profiles, the difference in the viscoelastic model's performance, when ignoring and  
369 considering the error bars, changes from ~86% to ~100% for TOT, increases from ~76% to ~87% for MU, and  
370 remains unchanged at 100% for REN.

371 Determining model's accuracy as the percentage of DInSAR measurements that fall inside the domain of a  
372 corresponding model, for the viscoelastic model, REN consistently demonstrates 100% accuracy regardless of whether  
373 the 'extra' profiles are considered, and whether error bars are included or not. For TOT, the accuracy remains at 100%  
374 when the error bars are included, with or without the 'extra' profiles, while without the measurements' error bars, the  
375 'extra' profiles improve accuracy by only ~2%. For MU, the inclusion of the 'extra' profiles results in a ~5% accuracy  
376 increase without the error bars, and a ~3% increase with the error bars. Conversely, for the viscous model, the  
377 inclusion of the 'extra' profiles improves the accuracy only for TOT: without the 'extra' profiles, the accuracy improves  
378 by ~8% and ~12% with and without the error bars, respectively. However, the accuracy of the viscous model  
379 decreases by ~6% and ~8% for REN and TOT, respectively, when the 'extra' profiles are removed and the  
380 measurements' error bars are considered. Thus, discarding the 'extra' profiles does not significantly enhance the  
381 models' performances and may even reduce the percentage of successfully modeled measurements in some cases.

382 Overall, considering all three glaciers together and accounting for all 80 profiles, the viscous model achieves ~16%  
383 or ~41% accuracy without or with the measurements error bars, respectively, while the viscoelastic model achieves  
384 ~81% or ~91% accuracy without or with the measurements error bars, respectively. Excluding the 'extra' profiles, the  
385 accuracy of the viscous model improves from ~13% to ~46% when the measurements' error bars are considered,  
386 while the accuracy of the viscoelastic model changes from ~84% to ~93% when the measurements' error bars are  
387 taken into account. Therefore, excluding the 'extra' profiles and considering error bars, the viscoelastic model  
388 outperforms the viscous model by ~47%. However, without error bars, the viscoelastic model outperforms the viscous  
389 model by ~71%. This finding underscores the critical importance of incorporating the elastic component in Stokes-  
390 based fluid glacier formulations.



391

392 **Figure 4.** Modeling results of (a) viscous and (b) viscoelastic models, averaged by the thickness values, with error  
 393 bars, representing the distance between the averaged grounding zone width for given thickness and  
 394 maximum/minimum grounding zone (GZ) values for this thickness but different inflow speed values. (c) comparison  
 395 of the modelling results (pink and green areas) with the DInSAR grounding zone measurements, where empty markers  
 396 show grounding zones obtained along ‘extra’ profiles from Table S2; (d) correlation plot of the modelling results.

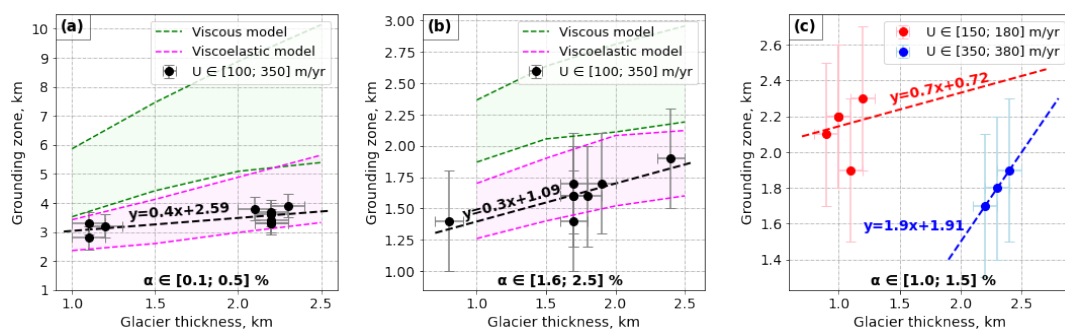
## 397 6. Conclusion

398 The variational formulation described in this paper has been successfully applied to the modeling of viscous and  
 399 viscoelastic glaciers on prograde bedrock slopes. In the investigated models, a thin water layer propagates into the gap  
 400 between the lower glacier surface and the bedrock, which forms due the impact of tidal forces. This gap formation  
 401 leads to the inland movement of the grounding line, resulting in the formation of a grounding zone, which represents  
 402 the magnitude of tide-induced grounding line migration over one tidal cycle. To compute the grounding zone width,  
 403 the viscoelastic and viscous models both require bed slope, glacier thickness, and glacier flow speed as input  
 404 parameters. Considering the grounding zone dependence on these parameters, several conclusions have emerged.





405 Firstly, the grounding zone widens as the bed slope becomes shallower, which is consistent with previous  
 406 observational studies (Milillo et al., 2017, 2019, 2022; Chen et al., 2023b). Secondly, for a given bed slope, the  
 407 grounding zone is wider for a thicker glacier, which is not only evident from the modeling results but is also supported  
 408 by the DInSAR measurements (Figure 5 a and b). Considering DInSAR measurements characterized by bed slopes  
 409 ranging from 0.1% to 0.5% and ice flow speeds ranging from 100 to 350 m/year and overlaying them with modelling  
 410 results obtained for the same range of bed slopes and flow speeds, we obtain a linear correlation between glacier  
 411 thickness and grounding zone width (Figure 5 a). Analogously, in Figure 5 b, a similar linear relationship between  
 412 glacier thickness and grounding zone is observed for the same range of glacier flow speeds and bed slopes ranging  
 413 from 1.6% to 2.5%. The range of slopes was increased compared to Figure 5 a as the grounding zone sensitivity to  
 414 variations in bed slopes decreases when bed becomes steeper, according to the first conclusion we made. Lastly, it can  
 415 be concluded from the modeled grounding zones that on steep bed slopes, the grounding zone is more responsive to  
 416 changes in glacier thickness when ice flow is slow; on shallow (mostly flat) bedrocks, the grounding zone is more  
 417 sensitive to variations in ice thickness if a glacier is flowing rapidly. Confirmation of this modelling result over shallow  
 418 slopes using DInSAR data is shown in Figure 5 c, where measurements characterized by faster ice flow exhibit a  
 419 steeper dependence of grounding zone width on glacier thickness compared to slower glacier flow. However, due to  
 420 the sparseness of the DInSAR dataset at steeper slopes, we cannot confirm the modeling-derived conclusion for steep  
 421 sloped bedrock.



422

423 **Figure 5.** Relationship between glacier thickness and DInSAR-derived grounding zone width. (a) DInSAR  
 424 measurements of grounding zone width (black dots) conducted along profiles characterized by bed slopes ranging  
 425 from 0.1 to 0.5% and ice flow speeds from 100 to 350 m/year. The black dashed line describes shows the linear  
 426 correlation between the ice thickness and DInSAR-derived grounding zones. The green and pink areas represent the  
 427 grounding zones calculated by the viscous and viscoelastic models, respectively, using the same range of bed slopes  
 428 and flow speeds as input parameters. (b) The black dots and the dashed line correspond to DInSAR measurements  
 429 described by bed slopes ranging from 1.6 to 2.5% and ice flow speeds from 100 to 350 m/year, and their linear  
 430 approximation, respectively. The green and pink areas correspond to the grounding zones, calculated by the viscous  
 431 and viscoelastic models, respectively, for the same range of bed slopes and flow speeds. (c) Grounding zone  
 432 measurements over 1.0 to 1.5% bed slopes, described by [150; 180] m/year and [350; 380] m/year ice flow speeds  
 433 with corresponding linear approximations.



434 Comparing all grounding zone values generated by the viscous and viscoelastic models, we observe a linear  
435 relationship between these values, with the grounding zone width obtained from the viscous model being  
436 approximately twice that calculated by the viscoelastic model across varying bedrock slopes, glacier thicknesses, and  
437 ice inflow speeds. To validate the models' performance, we compare their grounding zone outputs with DInSAR-  
438 derived grounding zones over Moscow University, Totten, and Rennick glaciers. To ensure the fair comparison of the  
439 models' outputs and the measurements, we input identical bed slope, glacier thickness, and glacier flow speed as those  
440 corresponding to these three glaciers and account for respective errors.

441 Comparison of the grounding zones, obtained from the DInSAR interferograms, with the modeled grounding zones  
442 shows that the viscoelastic model achieves significantly higher accuracy than the viscous model. Accounting for the  
443 error bars of the DInSAR measurements, the viscoelastic model successfully reproduced ~93% of all the  
444 measurements, while the viscous model succeeds with ~46% of the measurements. If the error bars are not considered,  
445 ~84% versus ~13% of the measurements are replicated by the viscoelastic and viscous model, respectively. Therefore,  
446 the accuracy of the viscoelastic model outperforms the accuracy of the viscous model by up to ~71%. Notably, the  
447 viscoelastic model reproduces all the measurements over Rennick glacier, either with or without the error bars, while  
448 the viscous model fails to replicate a single Rennick grounding zone measurement when the error bars are not included.  
449 These observations highlight the significance of incorporating the elastic component in Stokes-based glacier modeling  
450 compared to a purely viscous model.

451 Significant difference between viscous and viscoelastic models can be explained from a continuum mechanics  
452 perspective. Viscous response to deformation occurs over long timescales and corresponds to gradual deformations.  
453 However, a tidal impact occurs within a single day, rendering tide-induced deformations too rapid for accurate  
454 representation by a purely viscous model. Therefore, an element responsible for rapid deformations, or an elastic  
455 component, becomes necessary. Putting the viscous and elastic components in series, known as the Maxwell model  
456 of viscoelasticity, we ensure that both slow and rapid deformations are taken into account. However, the simple  
457 Maxwell model describes small deformations, whereas the deformations of our interest may extend up to 50% of the  
458 glacier domain length. Therefore, we applied the upper-convected Maxwell model of viscoelasticity, which includes  
459 some geometrical non-linearity and allows the modelling of significantly larger deformations compared to the simple  
460 Maxwell model.

461 Finally, (Li et al., 2023) mention that both ICESat laser altimetry and Sentinel-1a/b three-image DInSAR  
462 interferometry failed to delineate main trunk of TOT glacier and the central part of the MU main trunk due to the fast  
463 ice flow in these regions. On the contrary, the four-image CSK DInSAR technique utilized in this study allowed us to  
464 map grounding lines even over these fast-flowing areas. (Li et al., 2023) estimated the average grounding line retreat  
465 between 1996 and 2020 as  $3.51 \pm 0.49$  km for the southern lobe of the TOT main trunk, and as 13.85 km and 9.37 km  
466 for the western and eastern flanks of the MU main trunk, respectively. As, according to (Li et al., 2023), it is impossible  
467 to determine the magnitude of tidally induced grounding line migrations in 1996 from the historic grounding line  
468 dataset (Rignot et al., 2016), we assume the 1996 grounding line position as the average position between high and  
469 low tides. To calculate the long-term retreat, we estimate the distance from the historic grounding line to the center of  
470 the DInSAR-derived grounding zones for each glacier of interest. As a result, for MU, between 1996 and 2021, we



471 detect an average retreat of the main trunk of  $9 \pm 2$  km, with  $18 \pm 1$  km retreat at the western flank,  $6.7 \pm 0.6$  km retreat  
 472 at the central part of the main trunk, and  $4.2 \pm 0.6$  km retreat at the eastern flank. Therefore, the western flank  
 473 demonstrates the highest retreat rate of  $690 \pm 40$  m/year, while the average glacier retreat rate over this period was  
 474  $340 \pm 80$  m/year. For TOT, between 1996 and 2020, we observe an average retreat of the main trunk of  $9 \pm 3$  km with  
 475  $13.9 \pm 0.1$  km retreat at the western flank,  $17 \pm 1$  km retreat at the central part of the main trunk, and  $5.2 \pm 0.3$  km  
 476 retreat at the eastern flank. Therefore, while the average rate of TOT retreat between 1996 and 2020 was  
 477  $360 \pm 120$  m/year, the central part of the main trunk retreated as fast as  $680 \pm 40$  m/year. In the meantime, the position  
 478 of the REN grounding line at the main trunk did not change between 2000 and 2020, which signifies the stability of  
 479 the glacier over the past 20 years.

#### 480 **Appendix A: Glacier modelling**

481 Here, we provide a detailed description of the viscoelastic model and compare it with the viscous model.

##### 482 **A1. Principal notation**

483 Notation, used in the paper, is listed in Table A1.

484

**Table A1.** Models' principal notation

Symbol	Quantity
Geometry-related quantities	
$(X, Y)$	laboratory coordinate system
$x = (x, y)$	spatial point with coordinates $x$ and $y$
$\Omega$	glacier domain
$\partial\Omega$	boundary of the glacier domain
$\Gamma_D$	inflow boundary
$\Gamma_N$	outflow boundary
$\Gamma_a$	ice–air surface
$\Gamma_b$	ice–bedrock surface
$\Gamma_w$	ice–water surface
$\Gamma_s$	lower glacier boundary
$h(x, t)$	surface elevation of the ice shelf
$s(x, t)$	lower boundary of the ice shelf
$\alpha$	bedrock slope
$b(x)$	bedrock slope function
$A$	bedrock inclination parameter
$L$	glacier length
$H$	glacier thickness
$l$	sea level
Materials properties	
$\rho_i$	ice density
$\rho_w$	water density
$\phi$	friction
$C$	friction coefficient
$\eta$	ice viscosity
$G$	sheer modulus



$\lambda$	relaxation time
$r$	stress exponent (from the Glen's flow law)
$A$	ice softness
Scalar quantities	
$t$	time
$p$	ice pressure
$p_w$	water pressure at the ice–water interface
$p_w^0$	hydrostatic water pressure
$v_0$	inflow speed on $\Gamma_D$
Vector quantities	
$\hat{n}(\mathbf{x})$	unit outward normal vector at point $\mathbf{x}$ of a domain boundary
$\mathbf{v}$	ice flow velocity
$\mathbf{b}$	body force
$\mathbf{g}$	acceleration due to gravity
Tensor quantities	
$\mathbb{I}$	identity tensor
$\mathbb{P}$	orthogonal projection onto the boundary
$\mathbf{D}$	strain rate tensor
$\mathbf{T}$	Cauchy stress tensor
$\boldsymbol{\tau}$	deviatoric stress tensor
Mathematical operators	
$\nabla$	spatial gradient operator
$\nabla \cdot$	spatial divergence operator
$\cdot$	inner (dot) product
$\otimes$	tensor product
$\frac{\nabla}{\tau}$	upper-convected time derivative of some tensor field (in this case, of the tensor $\boldsymbol{\tau}$ )
Model parameters	
$\delta \ll 1$	Glen's flow law parameter numerical parameter, used to prevent model numerical instabilities
$B$	Glen's flow law parameter

## 485 A2. Model formulation

486 Using the notation provided in Table A1, we describe the formulation of both models, which have the same domain  
487 (see Viscous and viscoelastic models) and boundary conditions, but different governing equations.

### 488 A2.1. Governing equations

489 In both models, a glacier behaves as an incompressible non-Newtonian fluid, either viscous or viscoelastic.  
490 Incompressibility implies that the fluid density does not change during flow, which is mathematically infers zero  
491 divergence of the flow velocity  $\mathbf{v}$ :

$$\nabla \cdot \mathbf{v} = 0. \quad (\text{A1})$$

492 Both models are described by the Cauchy's first law of motion under quasi-static conditions, which provides the  
493 momentum conservation, and is identified as:

$$\nabla \cdot \mathbf{T}(\mathbf{v}, p) + \rho_i \mathbf{g} = 0, \quad (\text{A2})$$

494 where  $\mathbf{T}$  is the Cauchy stress tensor,  $\rho_i$  is the ice density, and  $\mathbf{g}$  is vector of gravitational acceleration, which in the  
495 glacier reference system is identified as  $\mathbf{g} = g(0 \quad -1)^T$  with magnitude  $g$ .



496 The difference between the models becomes apparent when considering the constitutive law, defining the physical  
497 nature of the models. The viscous model is described by the following equation:

$$\mathbf{T}(\mathbf{v}, p) = -p\mathbb{I} + 2\eta(\mathbf{v})\mathbf{D}, \quad (\text{A3})$$

498 where  $p$  is the ice pressure,  $\mathbb{I}$  is a second-order identity tensor,  $\eta(\mathbf{v})$  is a velocity-dependent ice viscosity, and  $\mathbf{D}$  is a  
499 strain rate tensor

$$\mathbf{D}(\mathbf{v}) = \frac{1}{2}[\nabla\mathbf{v} + (\nabla\mathbf{v})^T]. \quad (\text{A4})$$

500 Ice viscosity in the viscous model is identified via Glen's flow as

$$\eta(\mathbf{v}) = 2^{\frac{-1-n}{2n}} \cdot {}^{-n}\sqrt{A(|\mathbf{D}(\mathbf{v})|^2 + \delta)^{\frac{1-n}{2n}}}, \quad (\text{A5})$$

501 where  $n \geq 1$  is the stress exponent,  $A > 0$  is the ice softness, and  $\delta \ll 1$  is an infinitesimal numerical parameter, used  
502 to prevent numerical instability of the models at zero strain rate.

503 For the viscoelastic model, constitutive law (A3) and the viscosity expression (A5) are principally different. We  
504 consider the Maxwell model of viscoelasticity, which considers both viscous and elastic components assuming that  
505 deformation properties can be represented by a purely elastic spring and a purely viscous dashpot connected in series.  
506 Therefore, in the Maxwell model, a viscoelastic material behaves as a purely viscous flow under slow deformation  
507 (long timescale), while it exhibits elastic resistance to rapid deformations (short timescale). However, as the simple  
508 Maxwell model describes small deformations, we, apply the upper-convected Maxwell model instead, which includes  
509 some geometrical non-linearity. The constitutive relation for the viscoelastic model is identified as

$$\mathbf{T}(\mathbf{v}, p) = -p\mathbb{I} + \boldsymbol{\tau}, \quad (\text{A6})$$

510 where, compared to the purely viscous model (A3), the strain rate tensor  $\mathbf{D}$  (equation (A4)) is replaced with the  
511 deviatoric stress tensor  $\boldsymbol{\tau}$ , which is strain rate-dependent:

$$\boldsymbol{\tau} + \lambda \overset{\nabla}{\boldsymbol{\tau}} - 2\eta(\boldsymbol{\tau})\mathbf{D}(\mathbf{v}) = 0, \quad (\text{A7})$$

512 where  $\lambda = \frac{\eta(\boldsymbol{\tau})}{G}$  is the relaxation time with the shear modulus  $G$ , and the ice viscosity is

$$\eta(\boldsymbol{\tau}) = \frac{1}{2A|\boldsymbol{\tau}|^{n-1}}. \quad (\text{A8})$$

513  $\overset{\nabla}{\boldsymbol{\tau}}$  represents the upper-convected time derivative of  $\boldsymbol{\tau}$ :

$$\overset{\nabla}{\boldsymbol{\tau}} = \frac{D\boldsymbol{\tau}}{Dt} - (\nabla\mathbf{v})^T \cdot \boldsymbol{\tau} - \boldsymbol{\tau} \cdot \nabla\mathbf{v}, \quad (\text{A9})$$

514 where  $\frac{D\boldsymbol{\tau}}{Dt} = \frac{\partial\boldsymbol{\tau}}{\partial t} + \mathbf{v}\nabla\boldsymbol{\tau}$  is the material derivative of  $\boldsymbol{\tau}$ . Partial time derivative of  $\boldsymbol{\tau}$  on the current time step is calculated  
515 in the model through the previous time step using backward Euler approximation:

$$\frac{\partial\boldsymbol{\tau}(x, t)}{\partial t} = \frac{\boldsymbol{\tau}(x, t) - \boldsymbol{\tau}(x, t - \Delta t)}{\Delta t}. \quad (\text{A10})$$

## 516 A2.2. Evolution of the lower boundary

517 The time evolution of the lower boundary  $y = s(x, t)$  is governed by the kinematic equation, which expresses the fact  
518 that the surface moves with the ice flow, and under the assumption that there are no mass changes at the lower surface,  
519 such as melting or freezing, can be written as (Hirt and Nichols, 1981; Schoof, 2011)



$$\frac{\partial s}{\partial t} + v_x \frac{\partial s}{\partial x} = v_y, \quad (\text{A11})$$

520 where  $v_x$  and  $v_y$  are the components of the surface velocity vector  $\mathbf{v}|_s = (v_x, v_y)^T$ . Rewriting equation (A11) in terms

521 of the outward-pointing normal to the lower boundary  $\hat{\mathbf{n}}|_s = \frac{(\frac{\partial s}{\partial x} - 1)^T}{\sqrt{1 + (\frac{\partial s}{\partial x})^2}}$ , we get

$$\frac{\partial s}{\partial t} = -\mathbf{v} \cdot \hat{\mathbf{n}}|_s \cdot \sqrt{1 + \left(\frac{\partial s}{\partial x}\right)^2}. \quad (\text{A12})$$

522 As the solution of equation (A12) is numerically unstable (Durand et al., 2009b), we apply the backward Euler method  
523 to get rid of the instability. Denoting the approximate solution on  $k$ -th time step as  $s_*$ , such as  $s_* \equiv s(x, t_k)$ , and

524 applying the backward Euler method to equation (A12) under the assumption that  $\left(\frac{\partial s}{\partial x}\right)^2 \ll 1$ , we get

$$s_*(x, t_k) = s(x, t_k - \Delta t) - \Delta t \cdot v_n(x, s, t_k), \quad (\text{A13})$$

525 where  $\mathbf{v} \cdot \hat{\mathbf{n}}|_s$  was replaced with  $v_n$ . We assume that the ocean is hydrostatic and define  $p_w$  as the water pressure at  
526 the ice–water interface and  $p_w^0$  as the hydrostatic water pressure. If  $l$  is sea level, the hydrostatic water pressure at  $k$ -  
527 th time step is governed by the following equation:

$$p_w^0(x, s, t_k) = p_w g(l(t_k) - s_*(x, t_k)). \quad (\text{A14})$$

### 528 A2.3. Boundary conditions

529 Identifying  $\hat{\mathbf{n}}(\mathbf{x})$  as a unit outward normal vector at some point  $\mathbf{x}$  of any domain boundary, we determine an orthogonal  
530 projection onto that boundary as a second-order tensor  $\mathbb{P}$ :

$$\mathbb{P} := \mathbb{I} - \hat{\mathbf{n}}(\mathbf{x}) \otimes \hat{\mathbf{n}}(\mathbf{x}), \quad (\text{A15})$$

531 where  $\otimes$  is the tensor product. Denoting  $\cdot$  as an inner product, we also define the projection of the Cauchy stress tensor  
532  $\mathbf{T}$  as

$$T_n = -\hat{\mathbf{n}} \cdot \mathbf{T} \cdot \hat{\mathbf{n}}. \quad (\text{A16})$$

533 Both models use the same Dirichlet boundary conditions provided in Table A2, where  $v_0 > 0$  is the horizontal ice  
534 flow speed on the inflow boundary  $\Gamma_D$ .

535

**Table A2.** Models' boundary conditions

Boundary	Boundary condition	Physical meaning of a boundary condition	Equation number
$\Gamma_w$	$\mathbf{T} \cdot \hat{\mathbf{n}} = -p_w \hat{\mathbf{n}}$	Stress continuity at the ice–water boundary	(A17)
$\Gamma_a$	$\mathbf{T} \cdot \hat{\mathbf{n}} = 0$	No stress at the ice–air boundary	(A18)
$\Gamma_D$	$\begin{cases} v_x = v_0 \\ \mathbb{P} \mathbf{T} \hat{\mathbf{n}} = 0 \end{cases}$	On the inflow boundary the horizontal velocity is uniform and there is no vertical shear stress	(A19)
$\Gamma_N$	$\mathbf{T} \cdot \hat{\mathbf{n}} = -\rho_i g(h - y) \hat{\mathbf{n}}$	Cryostatic normal-stress condition on the outflow boundary	(A20)
$\Gamma_b$	$\mathbb{P} \mathbf{T} \hat{\mathbf{n}} + \phi(\mathbf{v}) \mathbb{P} \mathbf{v} = 0^*$	Sliding law on the ice-bed boundary	(A21)
$\Gamma_b$	$\begin{cases} T_n \geq p_w \\ v_n \leq 0 \\ (T_n - p_w)v_n = 0 \end{cases}$	There are three possibilities for the normal stress and the normal velocity component on the ice-bed boundary:	(A22)



		<p>(1) The normal stress exceeds the water pressure (<math>T_n &gt; p_w</math>) and the ice is not lifted off of the bed (<math>v_n = 0</math>);</p> <p>(2) The normal stress equals the water pressure (<math>T_n = p_w</math>) and the ice is lifted from the bed (<math>v_n &lt; 0</math>);</p> <p>(3) The normal stress equals the water pressure (<math>T_n = p_w</math>), but the ice is not lifted from the bed (<math>v_n = 0</math>).</p>	
<p>* in equation (A21), <math>\phi(\mathbf{v}) = C( \mathbb{P}\mathbf{v} ^2 + \delta)^{\frac{1-n}{2n}}</math> is friction with friction coefficient <math>C</math></p>			

536 **A3. Weak formulation**

537 In this subsection we provide the derivation of the viscoelastic model, while the viscous model is derived in  
538 (Stubblefield et al., 2021).

539 **A3.1. Mixed formulation**

540 Let us define  $V$  as the velocity function space.  $K$  is a closed, convex subset of  $V$  such that

$$K = \{\mathbf{v} \in V: v_n|_{\Gamma_b} \leq 0 \text{ and } v_x|_{\Gamma_D} = v_0\} \quad (\text{A23})$$

541 Multiplying equation (A2) by  $\mathbf{v} - \mathbf{u}$  (where  $\mathbf{u} \in K$  is an arbitrary test function), and integrating the expression over  
542 the glacier domain  $\Omega$ , in the indicial notation we will get:

$$\int_{\Omega} (v_k - u_k) T_{kj,j} dV + \int_{\Omega} \rho_i g_k (v_k - u_k) dV = 0. \quad (\text{A24})$$

543 Integrating the first integral in equation (A24) by parts and applying the divergence theorem (Green's identity), we  
544 then apply equation (A6) to one of the integrals and rewrite the resulting expression in tensor notation:

$$-\int_{\partial\Omega} \mathbf{T} \cdot \hat{\mathbf{n}} \cdot (\mathbf{v} - \mathbf{u}) da + \int_{\Omega} \{-p\nabla \cdot (\mathbf{v} - \mathbf{u}) + \boldsymbol{\tau} \cdot \nabla(\mathbf{v} - \mathbf{u}) - \rho_i g(\mathbf{v} - \mathbf{u})\} dV = 0. \quad (\text{A25})$$

545 Now we decompose  $\partial\Omega$  onto the compounding boundaries (see equation (2)) and consider the first integral in  
546 equation (A25) over each boundary separately. Using equations (A15), (A16), and boundary condition (A21) on  $\Gamma_b$ ,  
547 after integration over  $\Gamma_b$  and taking into account that  $T_n \geq p_w$  on  $\Gamma_b$ , we derive that

$$-\int_{\Gamma_b} \mathbf{T} \cdot \hat{\mathbf{n}} \cdot (\mathbf{v} - \mathbf{u}) da \leq \int_{\Gamma_b} \alpha(\mathbf{v}) \cdot \mathbb{P}\mathbf{v} \cdot \mathbb{P}(\mathbf{v} - \mathbf{u}) da + \int_{\Gamma_b} p_w (v_n - u_n) da. \quad (\text{A26})$$

548 On  $\Gamma_w$ , from equation (A17), we obtain the following expression:

$$-\int_{\Gamma_w} \mathbf{T} \cdot \hat{\mathbf{n}} \cdot (\mathbf{v} - \mathbf{u}) da = \int_{\Gamma_w} p_w (v_n - u_n) da. \quad (\text{A27})$$

549 On  $\Gamma_D$ , from equation (A19), we have  $\mathbb{P}\mathbf{T}\hat{\mathbf{n}} = 0$ , thus, this boundary does not contribute to the integral  
550  $\int_{\partial\Omega} \mathbf{T} \cdot \hat{\mathbf{n}} \cdot (\mathbf{v} - \mathbf{u}) da$ . On  $\Gamma_a$ , from equation (A18), we have  $\mathbf{T} \cdot \hat{\mathbf{n}} = 0$ , thus, this the ice-air boundary does not  
551 contribute to the integral  $\int_{\partial\Omega} \mathbf{T} \cdot \hat{\mathbf{n}} \cdot (\mathbf{v} - \mathbf{u}) da$  as well. On  $\Gamma_N$ , where from equation (A20), we know  $\mathbf{T} \cdot \hat{\mathbf{n}} =$   
552  $-\rho_i g(h - y)\hat{\mathbf{n}}$ , which means that the contribution from the boundary to  $\int_{\partial\Omega} \mathbf{T} \cdot \hat{\mathbf{n}} \cdot (\mathbf{v} - \mathbf{u}) da$  will be

$$-\int_{\Gamma_N} \mathbf{T} \cdot \hat{\mathbf{n}} \cdot (\mathbf{v} - \mathbf{u}) da = \int_{\Gamma_N} \rho_i g(h - y)(v_n - u_n) da. \quad (\text{A28})$$



553 Substituting equations (A26) – (A28) to equation (A25), replacing the union of  $\Gamma_w$  and  $\Gamma_b$  with  $\Gamma_s$  and replacing  $p_w$   
 554 with  $p_w = \rho_w g(l - s + \Delta t \cdot v_n)$ , which was derived from equations (A13) and (A14), we obtain

$$\int_{\Omega} \{-p \nabla \cdot (\mathbf{v} - \mathbf{u}) + \boldsymbol{\tau} \cdot \nabla (\mathbf{v} - \mathbf{u}) - \rho_i g (\mathbf{v} - \mathbf{u})\} dV + \int_{\Gamma_N} \rho_i g (h - y) (v_n - u_n) da + \int_{\Gamma_b} \alpha(\mathbf{v}) \cdot \mathbb{P} \mathbf{v} \cdot \mathbb{P} (\mathbf{v} - \mathbf{u}) da + \int_{\Gamma_s} \rho_w g (l - s + \Delta t \cdot v_n) (v_n - u_n) da \geq 0. \quad (\text{A29})$$

555 We define  $Q$  as a function space for pressure ( $q \in Q$ ), and  $M$  as a function space for stress ( $\boldsymbol{\mu} \in M$ ). To shorten and  
 556 simplify the notation, we introduce following functions:

$$F(\boldsymbol{\tau}, \mathbf{v}, \mathbf{u}) = \int_{\Omega} \boldsymbol{\tau} \cdot \nabla \mathbf{u} - \rho_i g \mathbf{u} dV + \int_{\Gamma_N} \rho_i g (h - y) u_n da + \int_{\Gamma_b} \alpha(\mathbf{v}) \cdot \mathbb{P} \mathbf{v} \cdot \mathbb{P} \mathbf{u} da \quad (\text{A30})$$

$$P(\mathbf{v}, \mathbf{u}) = \int_{\Gamma_s} \rho_w g (l - s + \Delta t \cdot v_n) u_n da \quad (\text{A31})$$

$$d_{\Omega}(\boldsymbol{\mu}, \boldsymbol{\tau}, \mathbf{v}) = \int_{\Omega} \boldsymbol{\mu} \left( \boldsymbol{\tau} + \frac{\eta}{G} \boldsymbol{\tau} - 2\eta D(\mathbf{v}) \right) dV \quad (\text{A32})$$

$$b_{\Omega}(q, \mathbf{v}) = \int_{\Omega} q \nabla \cdot \mathbf{v} dV \quad (\text{A33})$$

557 Writing inequality (A29) in terms of equations (A30) – (A33), we obtain

$$\begin{cases} F(\boldsymbol{\tau}, \mathbf{v}, \mathbf{v} - \mathbf{u}) + P(\mathbf{v}, \mathbf{v} - \mathbf{u}) - b_{\Omega}(p, \mathbf{v} - \mathbf{u}) \geq 0 \\ d_{\Omega}(\boldsymbol{\mu}, \boldsymbol{\tau}, \mathbf{v}) = 0 \\ b_{\Omega}(q, \mathbf{v}) = 0 \end{cases} \quad (\text{A34})$$

558 By analogy with (Stubblefield et al., 2021), we replace the mixed formulation (A34) with a penalty formulation

$$\begin{cases} F(\boldsymbol{\tau}, \mathbf{v}, \mathbf{u}) + P(\mathbf{v}, \mathbf{u}) - b_{\Omega}(p, \mathbf{u}) + \frac{\Pi'(\mathbf{v}, \mathbf{u})}{\epsilon} = 0 \\ d_{\Omega}(\boldsymbol{\mu}, \boldsymbol{\tau}, \mathbf{v}) = 0 \\ b_{\Omega}(q, \mathbf{v}) = 0 \end{cases} \quad (\text{A35})$$

559 Therefore, the penalized problem for the viscoelastic model is to find  $(\mathbf{v}, p, \boldsymbol{\tau}) \in V \times Q \times M$ , which satisfies the  
 560 boundary conditions and the system (A35).

### 561 Code and Data availability

562 All data needed to evaluate the conclusions in the paper are present in the paper and/or the Supplementary Materials.  
 563 We thank the Italian Space Agency (ASI) for providing CSK data (original COSMO-SkyMed product ASI, Agenzia  
 564 Spaziale Italiana (2008–2023)). Velocity (<https://nsidc.org/data/NSIDC-0484/versions/2>) and BedMachine  
 565 (<https://nsidc.org/data/NSIDC-0756/versions/2>) data products are available as MEaSURES products at the National  
 566 Snow and Ice Data Center, Boulder CO (NSIDC). The source codes for the viscous and viscoelastic models are freely  
 567 available on <https://github.com/agstub/grounding-line-methods/tree/v1.0.0> and  
 568 <https://github.com/agstub/viscoelastic-glines> GitHub repositories, respectively. Geocoded interferograms and  
 569 grounding-line positions are available at <https://doi.org/10.5281/zenodo.10853336>.





570 **Author contribution**

571 PM and NM designed the study; AS developed the viscous and viscoelastic models; NM performed the codes  
572 modifications and grounding zone simulations under the supervision of KN and RB; NM and PM performed the  
573 measurement of the grounding zones from the DInSAR data and the assessment of the main ice-bed system  
574 parameters; LD provided the CSK DInSAR data; NM and PN wrote the manuscript draft with contributions from KN,  
575 RB and AS reviewed and edited the manuscript.

576 **Competing interests**

577 The authors declare that they have no conflict of interest.

578 **Acknowledgements**

579 The research was conducted at the University of Houston, Houston, TX, US. We acknowledge the Research  
580 Computing Data Core (RCDC) for giving access to advance high-performance computing resources of the University  
581 of Houston. We thank the Italian Space Agency (ASI) for providing CSK data (original COSMO-SkyMed product  
582 ASI, Agenzia Spaziale Italiana (2008–2023)).

583 **References**

- 584 Van Achter, G., Fichefet, T., Goosse, H., Pelletier, C., Sterlin, J., Huot, P.-V., Lemieux, J.-F., Fraser, A. D., Haubner,  
585 K., and Porter-Smith, R.: Modelling landfast sea ice and its influence on ocean–ice interactions in the area of the  
586 Totten Glacier, East Antarctica, *Ocean Model (Oxf)*, 169, 101920, <https://doi.org/10.1016/j.ocemod.2021.101920>,  
587 2022.
- 588 Aitken, A. R. A., Roberts, J. L., Ommen, T. D. van, Young, D. A., Golledge, N. R., Greenbaum, J. S., Blankenship,  
589 D. D., and Siegert, M. J.: Repeated large-scale retreat and advance of Totten Glacier indicated by inland bed erosion,  
590 *Nature*, 533, 385–389, <https://doi.org/10.1038/nature17447>, 2016.
- 591 Albrecht, N., Vennell, R., Williams, M., Stevens, C., Langhorne, P., Leonard, G., and Haskell, T.: Observation of sub-  
592 inertial internal tides in McMurdo Sound, Antarctica, *Geophys Res Lett*, 33, <https://doi.org/10.1029/2006GL027377>,  
593 2006.
- 594 Allen, B., Mayewski, P. A., Lyons, W. B., and Spencer, M. J.: Glaciochemical Studies and Estimated Net Mass  
595 Balances for Rennick Glacier Area, Antarctica, *Ann Glaciol*, 7, 1–6, <https://doi.org/10.3189/S0260305500005826>,  
596 1985.
- 597 Alnæs, M., Blechta, J., Hake, J., Johansson, A., Kehlet, B., Logg, A., Richardson, C., Ring, J., Rognes, M. E., and  
598 Wells, G. N.: The FEniCS project version 1.5, *Archive of numerical software*, 3, 2015.
- 599 Begeman, C. B., Tulaczyk, S., Padman, L., King, M., Siegfried, M. R., Hodson, T. O., and Fricker, H. A.: Tidal  
600 Pressurization of the Ocean Cavity Near an Antarctic Ice Shelf Grounding Line, *J Geophys Res Oceans*, 125,  
601 e2019JC015562, <https://doi.org/10.1029/2019JC015562>, 2020.
- 602 Beldon, C. L. and Mitchell, N. J.: Gravity wave–tidal interactions in the mesosphere and lower thermosphere over  
603 Rothera, Antarctica (68°S, 68°W), *Journal of Geophysical Research: Atmospheres*, 115,  
604 <https://doi.org/10.1029/2009JD013617>, 2010.



- 605 Bensi, M., Kovačević, V., Donda, F., O'Brien, P. E., Armbrecht, L., and Armand, L. K.: Water masses distribution  
606 offshore the Sabrina Coast (East Antarctica), *Earth Syst Sci Data*, 14, 65–78, <https://doi.org/10.5194/essd-14-65-2022>,  
607 2022.
- 608 Brancato, V., Rignot, E., Milillo, P., Morlighem, M., Mouginot, J., An, L., Scheuchl, B., Jeong, S., Rizzoli, P.,  
609 Bueso Bello, J. L., and Prats-Iraola, P.: Grounding Line Retreat of Denman Glacier, East Antarctica, Measured With  
610 COSMO-SkyMed Radar Interferometry Data, *Geophys Res Lett*, 47, e2019GL086291,  
611 <https://doi.org/10.1029/2019GL086291>, 2020.
- 612 Brunt, K. M., Fricker, H. A., Padman, L., Scambos, T. A., and O'Neel, S.: Mapping the grounding zone of the Ross  
613 Ice Shelf, Antarctica, using ICESat laser altimetry, *Ann Glaciol*, 51, 71–79,  
614 <https://doi.org/10.3189/172756410791392790>, 2010.
- 615 Chen, H., Rignot, E., Scheuchl, B., and Ehrenfeucht, S.: Grounding Zone of Amery Ice Shelf, Antarctica, From  
616 Differential Synthetic-Aperture Radar Interferometry, *Geophys Res Lett*, 50, e2022GL102430,  
617 <https://doi.org/10.1029/2022GL102430>, 2023a.
- 618 Chen, H., Rignot, E., Scheuchl, B., and Ehrenfeucht, S.: Grounding Zone of Amery Ice Shelf, Antarctica, From  
619 Differential Synthetic-Aperture Radar Interferometry, *Geophys Res Lett*, 50, e2022GL102430,  
620 <https://doi.org/10.1029/2022GL102430>, 2023b.
- 621 Ciraci, E., Rignot, E., Scheuchl, B., Tolpekin, V., Wollersheim, M., An, L., Milillo, P., Bueso-Bello, J.-L., Rizzoli,  
622 P., and Dini, L.: Melt rates in the kilometer-size grounding zone of Petermann Glacier, Greenland, before and during  
623 a retreat, *Proceedings of the National Academy of Sciences*, 120, e2220924120,  
624 <https://doi.org/10.1073/pnas.2220924120>, 2023.
- 625 Coleman, R., Erofeeva, L., Fricker, H. A., Howard, S., and Padman, L.: A new tide model for the Antarctic ice shelves  
626 and seas, *Ann Glaciol*, 34, 247–254, [https://doi.org/DOI: 10.3189/172756402781817752](https://doi.org/DOI:10.3189/172756402781817752), 2002.
- 627 Cornford, S. L., Seroussi, H., Asay-Davis, X. S., Gudmundsson, G. H., Arthern, R., Borstad, C., Christmann, J., Dias  
628 dos Santos, T., Feldmann, J., Goldberg, D., Hoffman, M. J., Humbert, A., Kleiner, T., Leguy, G., Lipscomb, W. H.,  
629 Merino, N., Durand, G., Morlighem, M., Pollard, D., Rückamp, M., Williams, C. R., and Yu, H.: Results of the third  
630 Marine Ice Sheet Model Intercomparison Project (MISMIP+), *Cryosphere*, 14, 2283–2301, [https://doi.org/10.5194/tc-](https://doi.org/10.5194/tc-14-2283-2020)  
631 14-2283-2020, 2020.
- 632 Davis, P. E. D., Nicholls, K. W., Holland, D. M., Schmidt, B. E., Washam, P., Riverman, K. L., Arthern, R. J.,  
633 Vaňková, I., Eayrs, C., Smith, J. A., Anker, P. G. D., Mullen, A. D., Dichek, D., Lawrence, J. D., Meister, M. M.,  
634 Clyne, E., Basinski-Ferris, A., Rignot, E., Queste, B. Y., Boehme, L., Heywood, K. J., Anandakrishnan, S., and  
635 Makinson, K.: Suppressed basal melting in the eastern Thwaites Glacier grounding zone, *Nature*, 614, 479–485,  
636 <https://doi.org/10.1038/s41586-022-05586-0>, 2023.
- 637 Davison, B. J., Hogg, A. E., Rigby, R., Veldhuijsen, S., van Wessem, J. M., van den Broeke, M. R., Holland, P. R.,  
638 Selley, H. L., and Dutrieux, P.: Sea level rise from West Antarctic mass loss significantly modified by large snowfall  
639 anomalies, *Nat Commun*, 14, 1479, <https://doi.org/10.1038/s41467-023-36990-3>, 2023.
- 640 Dawson, G. J. and Bamber, J. L.: Antarctic Grounding Line Mapping From CryoSat-2 Radar Altimetry, *Geophys Res*  
641 *Lett*, 44, 11,886–11,893, <https://doi.org/10.1002/2017GL075589>, 2017.



- 642 Dempsey, S. M., Hindley, N. P., Moffat-Griffin, T., Wright, C. J., Smith, A. K., Du, J., and Mitchell, N. J.: Winds and  
643 tides of the Antarctic mesosphere and lower thermosphere: One year of meteor-radar observations over Rothera (68°S,  
644 68°W) and comparisons with WACCM and eCMAM, *J Atmos Sol Terr Phys*, 212, 105510,  
645 <https://doi.org/https://doi.org/10.1016/j.jastp.2020.105510>, 2021.
- 646 Durand, G., Gagliardini, O., Zwinger, T., Meur, E. Le, and Hindmarsh, R. C. A.: Full Stokes modeling of marine ice  
647 sheets: influence of the grid size, *Ann Glaciol*, 50, 109–114, <https://doi.org/10.3189/172756409789624283>, 2009a.
- 648 Durand, G., Gagliardini, O., de Fleurian, B., Zwinger, T., and Le Meur, E.: Marine ice sheet dynamics: Hysteresis and  
649 neutral equilibrium, *J Geophys Res*, 114, F03009, <https://doi.org/10.1029/2008JF001170>, 2009b.
- 650 Favier, L., Durand, G., Cornford, S. L., Gudmundsson, G. H., Gagliardini, O., Gillet-Chaulet, F., Zwinger, T., Payne,  
651 A. J., and Le Brocq, A. M.: Retreat of Pine Island Glacier controlled by marine ice-sheet instability, *Nat Clim Chang*,  
652 4, 117–121, <https://doi.org/10.1038/nclimate2094>, 2014.
- 653 Fernandez, R., Gulick, S., Domack, E., Montelli, A., Leventer, A., Shevenell, A., and Frederick, B.: Past ice stream  
654 and ice sheet changes on the continental shelf off the Sabrina Coast, East Antarctica, *Geomorphology*, 317, 10–22,  
655 <https://doi.org/10.1016/j.geomorph.2018.05.020>, 2018.
- 656 Freer, B. I. D., Marsh, O. J., Hogg, A. E., Fricker, H. A., and Padman, L.: Modes of Antarctic tidal grounding line  
657 migration revealed by Ice, Cloud, and land Elevation Satellite-2 (ICESat-2) laser altimetry, *Cryosphere*, 17, 4079–  
658 4101, <https://doi.org/10.5194/tc-17-4079-2023>, 2023.
- 659 Friedl, P., Weiser, F., Fluhrer, A., and Braun, M. H.: Remote sensing of glacier and ice sheet grounding lines: A  
660 review, *Earth Sci Rev*, 201, 102948, <https://doi.org/10.1016/j.earscirev.2019.102948>, 2020.
- 661 Gadi, R., Rignot, E., and Menemenlis, D.: Modeling Ice Melt Rates From Seawater Intrusions in the Grounding Zone  
662 of Petermann Gletscher, Greenland, *Geophys Res Lett*, 50, e2023GL105869, <https://doi.org/10.1029/2023GL105869>,  
663 2023.
- 664 Gagliardini, O., Brondex, J., Gillet-Chaulet, F., Tavard, L., Peyaud, V., and Durand, G.: Brief communication: Impact  
665 of mesh resolution for MISMIP and MISMIP3d experiments using Elmer/Ice, *Cryosphere*, 10, 307–312,  
666 <https://doi.org/10.5194/tc-10-307-2016>, 2016.
- 667 Goldstein, R. M., Engelhardt, H., Kamb, B., and Frolich, R. M.: Satellite Radar Interferometry for Monitoring Ice  
668 Sheet Motion: Application to an Antarctic Ice Stream, *Science* (1979), 262, 1525–1530,  
669 <https://doi.org/10.1126/science.262.5139.1525>, 1993.
- 670 Gudmundsson, G. H.: Ice-stream response to ocean tides and the form of the basal sliding law, *Cryosphere*, 5, 259–  
671 270, <https://doi.org/10.5194/tc-5-259-2011>, 2011.
- 672 Gudmundsson, G. H., Krug, J., Durand, G., Favier, L., and Gagliardini, O.: The stability of grounding lines on  
673 retrograde slopes, *Cryosphere*, 6, 1497–1505, <https://doi.org/10.5194/tc-6-1497-2012>, 2012.
- 674 Haseloff, M. and Sergienko, O. V.: The effect of buttressing on grounding line dynamics, *Journal of Glaciology*, 64,  
675 417–431, <https://doi.org/10.1017/jog.2018.30>, 2018.
- 676 Hibbins, R. E., Marsh, O. J., McDonald, A. J., and Jarvis, M. J.: A new perspective on the longitudinal variability of  
677 the semidiurnal tide, *Geophys Res Lett*, 37, <https://doi.org/10.1029/2010GL044015>, 2010.



- 678 Hirt, C. W. and Nichols, B. D.: Volume of fluid (VOF) method for the dynamics of free boundaries, *J Comput Phys*,  
679 39, 201–225, [https://doi.org/10.1016/0021-9991\(81\)90145-5](https://doi.org/10.1016/0021-9991(81)90145-5), 1981.
- 680 Holland, P. R.: A model of tidally dominated ocean processes near ice shelf grounding lines, *J Geophys Res Oceans*,  
681 113, <https://doi.org/10.1029/2007JC004576>, 2008.
- 682 Li, T., Dawson, G. J., Chuter, S. J., and Bamber, J. L.: Grounding line retreat and tide-modulated ocean channels at  
683 Moscow University and Totten Glacier ice shelves, East Antarctica, *Cryosphere*, 17, 1003–1022,  
684 <https://doi.org/10.5194/tc-17-1003-2023>, 2023.
- 685 Logg, A., Mardal, K.-A., and Wells, G.: Automated solution of differential equations by the finite element method:  
686 The FEniCS book, Springer Science & Business Media, 2012.
- 687 MacAyeal, D. R.: Large-scale ice flow over a viscous basal sediment: Theory and application to ice stream B,  
688 Antarctica, *J Geophys Res Solid Earth*, 94, 4071–4087, <https://doi.org/10.1029/JB094iB04p04071>, 1989.
- 689 Marsh, O. J., Fricker, H. A., Siegfried, M. R., Christianson, K., Nicholls, K. W., Corr, H. F. J., and Catania, G.: High  
690 basal melting forming a channel at the grounding line of Ross Ice Shelf, Antarctica, *Geophys Res Lett*, 43, 250–255,  
691 <https://doi.org/https://doi.org/10.1002/2015GL066612>, 2016.
- 692 Mayewski, P. A., Attig, J. W., and Drewry, D. J.: Pattern of Ice Surface Lowering for Rennick Glacier, Northern  
693 Victoria Land, Antarctica, *Journal of Glaciology*, 22, 53–65, <https://doi.org/10.3189/S0022143000014052>, 1979.
- 694 Meneghel, M., Bondesan, A., Salvatore, M. C., and Orombelli, G.: A model of the glacial retreat of upper Rennick  
695 Glacier, Victoria Land, Antarctica, *Ann Glaciol*, 29, 225–230, <https://doi.org/10.3189/172756499781821463>, 1999.
- 696 Miles, B. W. J., Stokes, C. R., Jamieson, S. S. R., Jordan, J. R., Gudmundsson, G. H., and Jenkins, A.: High spatial  
697 and temporal variability in Antarctic ice discharge linked to ice shelf buttressing and bed geometry, *Sci Rep*, 12,  
698 10968, <https://doi.org/10.1038/s41598-022-13517-2>, 2022.
- 699 Milillo, P., Fielding, E. J., Shulz, W. H., Delbridge, B., and Burgmann, R.: COSMO-SkyMed Spotlight Interferometry  
700 Over Rural Areas: The Slumgullion Landslide in Colorado, USA, *IEEE J Sel Top Appl Earth Obs Remote Sens*, 7,  
701 2919–2926, <https://doi.org/10.1109/JSTARS.2014.2345664>, 2014.
- 702 Milillo, P., Rignot, E., Mougnot, J., Scheuchl, B., Morlighem, M., Li, X., and Salzer, J. T.: On the Short-term  
703 Grounding Zone Dynamics of Pine Island Glacier, West Antarctica, Observed With COSMO-SkyMed Interferometric  
704 Data, *Geophys Res Lett*, 44, 10,436-10,444, <https://doi.org/10.1002/2017GL074320>, 2017.
- 705 Milillo, P., Rignot, E., Rizzoli, P., Scheuchl, B., Mougnot, J., Bueso-Bello, J., and Prats-Iraola, P.: Heterogeneous  
706 retreat and ice melt of Thwaites Glacier, West Antarctica, *Sci Adv*, 5, eaau3433,  
707 <https://doi.org/10.1126/sciadv.aau3433>, 2019.
- 708 Milillo, P., Rignot, E., Rizzoli, P., Scheuchl, B., Mougnot, J., Bueso-Bello, J. L., Prats-Iraola, P., and Dini, L.: Rapid  
709 glacier retreat rates observed in West Antarctica, *Nat Geosci*, 15, 48–53, [https://doi.org/10.1038/s41561-021-00877-](https://doi.org/10.1038/s41561-021-00877-z)  
710 z, 2022.
- 711 Minchew, B. M., Simons, M., Riel, B., and Milillo, P.: Tidally induced variations in vertical and horizontal motion on  
712 Rutford Ice Stream, West Antarctica, inferred from remotely sensed observations, *J Geophys Res Earth Surf*, 122,  
713 167–190, <https://doi.org/10.1002/2016JF003971>, 2017.



- 714 Mohajerani, Y., Velicogna, I., and Rignot, E.: Mass Loss of Totten and Moscow University Glaciers, East Antarctica,  
715 Using Regionally Optimized GRACE Mascons, *Geophys Res Lett*, 45, 7010–7018,  
716 <https://doi.org/10.1029/2018GL078173>, 2018.
- 717 Morlighem, M., Williams, C. N., Rignot, E., An, L., Arndt, J. E., Bamber, J. L., Catania, G., Chauché, N., Dowdeswell,  
718 J. A., Dorschel, B., Fenty, I., Hogan, K., Howat, I., Hubbard, A., Jakobsson, M., Jordan, T. M., Kjeldsen, K. K.,  
719 Millan, R., Mayer, L., Mouginot, J., Noël, B. P. Y., O’Cofaigh, C., Palmer, S., Rysgaard, S., Seroussi, H., Siegert, M.  
720 J., Slabon, P., Straneo, F., van den Broeke, M. R., Weinrebe, W., Wood, M., and Zinglensen, K. B.: BedMachine v3:  
721 Complete Bed Topography and Ocean Bathymetry Mapping of Greenland From Multibeam Echo Sounding Combined  
722 With Mass Conservation, *Geophys Res Lett*, 44, 11–51, <https://doi.org/10.1002/2017GL074954>, 2017.
- 723 Muszynski, I. and Birchfield, G. E.: A Coupled Marine Ice-Stream – Ice-Shelf Model, *Journal of Glaciology*, 33, 3–  
724 15, <https://doi.org/10.3189/S0022143000005281>, 1987.
- 725 Orsi, A. H. and Webb, C. J.: Impact of Sea Ice Production off Sabrina Coast, East Antarctica, *Geophys Res Lett*, 49,  
726 e2021GL095613, <https://doi.org/10.1029/2021GL095613>, 2022.
- 727 Padman, L., Siegfried, M. R., and Fricker, H. A.: Ocean Tide Influences on the Antarctic and Greenland Ice Sheets,  
728 *Reviews of Geophysics*, 56, 142–184, <https://doi.org/10.1002/2016RG000546>, 2018.
- 729 Pattyn, F., Schoof, C., Perichon, L., Hindmarsh, R. C. A., Bueler, E., de Fleurian, B., Durand, G., Gagliardini, O.,  
730 Gladstone, R., Goldberg, D., Gudmundsson, G. H., Huybrechts, P., Lee, V., Nick, F. M., Payne, A. J., Pollard, D.,  
731 Rybak, O., Saito, F., and Vieli, A.: Results of the Marine Ice Sheet Model Intercomparison Project, *MISMIP*,  
732 *Cryosphere*, 6, 573–588, <https://doi.org/10.5194/tc-6-573-2012>, 2012.
- 733 Pegler, S. S. and Worster, M. G.: An experimental and theoretical study of the dynamics of grounding lines, *J Fluid*  
734 *Mech*, 728, 5–28, <https://doi.org/10.1017/jfm.2013.269>, 2013.
- 735 Pegler, S. S., Kowal, K. N., Hasenclever, L. Q., and Worster, M. G.: Lateral controls on grounding-line dynamics, *J*  
736 *Fluid Mech*, 722, R1, <https://doi.org/10.1017/jfm.2013.140>, 2013.
- 737 Pritchard, H. D., Arthern, R. J., Vaughan, D. G., and Edwards, L. A.: Extensive dynamic thinning on the margins of  
738 the Greenland and Antarctic ice sheets, *Nature*, 461, 971–975, <https://doi.org/10.1038/nature08471>,  
739 2009.
- 740 Pritchard, H. D., Ligtenberg, S. R. M., Fricker, H. A., Vaughan, D. G., van den Broeke, M. R., and Padman, L.:  
741 Antarctic ice-sheet loss driven by basal melting of ice shelves, *Nature*, 484, 502–505,  
742 <https://doi.org/10.1038/nature10968>, 2012.
- 743 Rignot, E. and Thomas, R. H.: Mass Balance of Polar Ice Sheets, *Science* (1979), 297, 1502–1506,  
744 <https://doi.org/10.1126/science.1073888>, 2002.
- 745 Rignot, E., Jacobs, S., Mouginot, J., and Scheuchl, B.: Ice-Shelf Melting Around Antarctica, *Science* (1979), 341,  
746 266–270, <https://doi.org/10.1126/science.1235798>, 2013.
- 747 Rignot, E., Mouginot, J., Morlighem, M., Seroussi, H., and Scheuchl, B.: Widespread, rapid grounding line retreat of  
748 Pine Island, Thwaites, Smith, and Kohler glaciers, West Antarctica, from 1992 to 2011, *Geophys Res Lett*, 41, 3502–  
749 3509, <https://doi.org/10.1002/2014GL060140>, 2014.



- 750 Rignot, E., Mouginot, J., and Scheuchl, B.: MEaSURES Antarctic Grounding Line from Differential Satellite Radar  
751 Interferometry, Version 2, Nat. Snow and Ice Data Center, <https://doi.org/https://doi.org/10.5067/IKBWW4RYHF1Q>,  
752 2016.
- 753 Rignot, E., Mouginot, J., and Scheuchl, B.: MEaSURES InSAR-based Antarctica ice velocity map, version 2, Nat.  
754 Snow Ice Data Center, <https://doi.org/https://doi.org/10.5067/D7GK8F5J8M8R>, 2017.
- 755 Rignot, E., Mouginot, J., Scheuchl, B., van den Broeke, M., van Wessem, M. J., and Morlighem, M.: Four decades of  
756 Antarctic Ice Sheet mass balance from 1979–2017, *Proceedings of the National Academy of Sciences*, 116, 1095–  
757 1103, <https://doi.org/10.1073/pnas.1812883116>, 2019.
- 758 Roberts, J., Galton-Fenzi, B. K., Paolo, F. S., Donnelly, C., Gwyther, D. E., Padman, L., Young, D., Warner, R.,  
759 Greenbaum, J., Fricker, H. A., Payne, A. J., Cornford, S., Le Brocq, A., van Ommen, T., Blankenship, D., and Siegert,  
760 M. J.: Ocean forced variability of Totten Glacier mass loss, Geological Society, London, Special Publications, 461,  
761 175–186, <https://doi.org/10.1144/SP461.6>, 2018.
- 762 Robison, R. A. V., Huppert, H. E., and Worster, M. G.: Dynamics of viscous grounding lines, *J Fluid Mech*, 648, 363–  
763 380, <https://doi.org/10.1017/S0022112009993119>, 2010.
- 764 Rosier, S. H. R. and Gudmundsson, G. H.: Exploring mechanisms responsible for tidal modulation in flow of the  
765 Filchner–Ronne Ice Shelf, *Cryosphere*, 14, 17–37, <https://doi.org/10.5194/tc-14-17-2020>, 2020.
- 766 Rosier, S. H. R., Gudmundsson, G. H., and Green, J. A. M.: Insights into ice stream dynamics through modelling their  
767 response to tidal forcing, *Cryosphere*, 8, 1763–1775, <https://doi.org/10.5194/tc-8-1763-2014>, 2014.
- 768 Sayag, R. and Worster, M. G.: Elastic response of a grounded ice sheet coupled to a floating ice shelf, *Phys Rev E*,  
769 84, 036111, <https://doi.org/10.1103/PhysRevE.84.036111>, 2011.
- 770 Sayag, R. and Worster, M. G.: Elastic dynamics and tidal migration of grounding lines modify subglacial lubrication  
771 and melting, *Geophys Res Lett*, 40, 5877–5881, <https://doi.org/10.1002/2013GL057942>, 2013.
- 772 Schoof, C.: Ice sheet grounding line dynamics: Steady states, stability, and hysteresis, *J Geophys Res*, 112, F03S28,  
773 <https://doi.org/10.1029/2006JF000664>, 2007a.
- 774 Schoof, C.: Marine ice-sheet dynamics. Part 1. The case of rapid sliding, *J Fluid Mech*, 573, 27–55,  
775 <https://doi.org/10.1017/S0022112006003570>, 2007b.
- 776 Schoof, C.: Marine ice sheet dynamics. Part 2. A Stokes flow contact problem, *J Fluid Mech*, 679, 122–155,  
777 <https://doi.org/10.1017/jfm.2011.129>, 2011.
- 778 Sergienko, O. and Haseloff, M.: ‘Stable’ and ‘unstable’ are not useful descriptions of marine ice sheets in the Earth’s  
779 climate system, *Journal of Glaciology*, 69, 1483–1499, <https://doi.org/10.1017/jog.2023.40>, 2023.
- 780 Sergienko, O. V.: No general stability conditions for marine ice-sheet grounding lines in the presence of feedbacks,  
781 *Nat Commun*, 13, 2265, <https://doi.org/10.1038/s41467-022-29892-3>, 2022.
- 782 Seroussi, H., Morlighem, M., Larour, E., Rignot, E., and Khazendar, A.: Hydrostatic grounding line parameterization  
783 in ice sheet models, *Cryosphere*, 8, 2075–2087, <https://doi.org/10.5194/tc-8-2075-2014>, 2014.
- 784 Snoeijer, J. H., Pandey, A., Herrada, M. A., and Eggers, J.: The relationship between viscoelasticity and elasticity,  
785 *Proceedings of the Royal Society A: Mathematical, Physical and Engineering Sciences*, 476, 20200419,  
786 <https://doi.org/10.1098/rspa.2020.0419>, 2020.



- 787 Stubblefield, A. G., Spiegelman, M., and Creyts, T. T.: Variational formulation of marine ice-sheet and subglacial-  
788 lake grounding-line dynamics, *J Fluid Mech*, 919, A23, <https://doi.org/10.1017/jfm.2021.394>, 2021.
- 789 Sturm, A. and Carryer, S. J.: Geology of the region between the Matusевич and Tucker Glaciers, north Victoria Land,  
790 Antarctica, *New Zealand Journal of Geology and Geophysics*, 13, 408–435,  
791 <https://doi.org/10.1080/00288306.1970.10423977>, 1970.
- 792 Thomas, R. H. and Bentley, C. R.: A Model for Holocene Retreat of the West Antarctic Ice Sheet, *Quat Res*, 10, 150–  
793 170, [https://doi.org/10.1016/0033-5894\(78\)90098-4](https://doi.org/10.1016/0033-5894(78)90098-4), 1978.
- 794 Tsai, V. C. and Gudmundsson, G. H.: An improved model for tidally modulated grounding-line migration, *Journal of*  
795 *Glaciology*, 61, 216–222, <https://doi.org/10.3189/2015JoG14J152>, 2015.
- 796 Warburton, K. L. P., Hewitt, D. R., and Neufeld, J. A.: Tidal Grounding-Line Migration Modulated by Subglacial  
797 Hydrology, *Geophys Res Lett*, 47, e2020GL089088, <https://doi.org/10.1029/2020GL089088>, 2020.
- 798 Weertman, J.: Stability of the Junction of an Ice Sheet and an Ice Shelf, *Journal of Glaciology*, 13, 3–11,  
799 <https://doi.org/10.3189/S0022143000023327>, 1974.
- 800